

# WITNESSING THE BIRTH OF THE RED SEQUENCE: THE PHYSICAL SCALE AND MORPHOLOGY OF DUST EMISSION IN HYPER-LUMINOUS STARBURSTS IN THE EARLY UNIVERSE

I. OTEO,<sup>1,2</sup> R. J. IVISON,<sup>2,1</sup> M. NEGRELLO,<sup>3</sup> I. SMAIL,<sup>4,5</sup> I. PÉREZ-FOURNON,<sup>6,7</sup> M. BREMER,<sup>8</sup> G. DE ZOTTI,<sup>9</sup> S. A. EALES,<sup>3</sup> D. FARRAH,<sup>10</sup> P. TEMI,<sup>11</sup> D. L. CLEMENTS,<sup>12</sup> A. COORAY,<sup>13</sup> H. DANNERBAUER,<sup>6,7</sup> S. DUIVENVOORDEN,<sup>14</sup> L. DUNNE,<sup>1,3</sup> E. IBAR,<sup>15</sup> A. J. R. LEWIS,<sup>1</sup> R. MARQUES-CHAVES,<sup>6,7</sup> P. MARTÍNEZ-NAVAJAS,<sup>6,7</sup> M. J. MICHAŁOWSKI,<sup>16</sup> A. OMONT,<sup>17,18</sup> S. OLIVER,<sup>14</sup> D. RIECHERS,<sup>19</sup> D. SCOTT<sup>20</sup> AND P. VAN DER WERF<sup>21</sup>

<sup>1</sup>Institute for Astronomy, University of Edinburgh, Royal Observatory, Blackford Hill, Edinburgh EH9 3HJ, U.K.

<sup>2</sup>European Southern Observatory, Karl-Schwarzschild-Str. 2, 85748 Garching, Germany

<sup>3</sup>School of Physics & Astronomy, Cardiff University, Queen's Buildings, The Parade, Cardiff CF24 3AA, U.K.

<sup>4</sup>Centre for Extragalactic Astronomy, Department of Physics, Durham University, South Road, Durham DH1 3LE, U.K.

<sup>5</sup>Institute for Computational Cosmology, Department of Physics, Durham University, South Road, Durham DH1 3LE, U.K.

<sup>6</sup>IAC, E-38200 La Laguna, Tenerife, Spain

<sup>7</sup>Departamento de Astrofísica, Universidad de La Laguna, E-38205 La Laguna, Tenerife, Spain

<sup>8</sup>H.H. Wills Physics Laboratory, University of Bristol, Tyndall Avenue, Bristol BS8 1TL, U.K.

<sup>9</sup>INAF, Osservatorio Astronomico di Padova, Vicolo Osservatorio 5, I-35122 Padova, Italy

<sup>10</sup>Department of Physics, Virginia Tech, Blacksburg, VA 24061

<sup>11</sup>Astrophysics Branch, NASA/Ames Research Center, MS 245-6, Moffett Field, CA 94035

<sup>12</sup>Physics Department, Blackett Lab, Imperial College, Prince Consort Road, London SW7 2AZ, U.K.

<sup>13</sup>Department of Physics and Astronomy, University of California, Irvine, CA 92697

<sup>14</sup>Astronomy Centre, Department of Physics and Astronomy, University of Sussex, Brighton BN1 9QH, U.K.

<sup>15</sup>Instituto de Física y Astronomía, Universidad de Valparaíso, Avda. Gran Bretaña 1111, Valparaíso, Chile

<sup>16</sup>Astronomical Observatory Institute, Faculty of Physics, Adam Mickiewicz University, ul. Słoneczna 36, 60-286 Poznań, Poland

<sup>17</sup>UPMC Univ Paris 06, UMR 7095, IAP, 75014, Paris, France

<sup>18</sup>CNRS, UMR7095, IAP, F-75014, Paris, France

<sup>19</sup>Cornell University, Space Sciences Building, Ithaca, NY 14853

<sup>20</sup>Department of Physics and Astronomy, University of British Columbia, 6224 Agricultural Road, Vancouver, BC V6T 1Z1, Canada and

<sup>21</sup>Leiden Observatory, Leiden University, P.O. Box 9513, NL-2300 RA Leiden, The Netherlands

*Draft version October 28, 2021*

## ABSTRACT

We present high-spatial-resolution ( $\sim 0.12''$  or  $\approx 800$  pc at  $z = 4.5$ ) ALMA 870  $\mu\text{m}$  dust continuum observations of a sample of 44 ultrared dusty star-forming galaxies (DSFGs) selected from the *H-ATLAS* and *HerMES* far-infrared surveys because of their red colors from 250 to 500  $\mu\text{m}$ :  $S_{500}/S_{250} > 1.5$  and  $S_{500}/S_{350} > 1.0$ . With photometric redshifts in the range  $z \sim 4-6$ , our sample includes the most luminous starbursting systems in the early Universe known so far, with total obscured star-formation rates (SFRs) of up to  $\sim 4,500 M_{\odot} \text{yr}^{-1}$ , as well as a population of lensed, less intrinsically luminous sources. The lower limit on the number of ultrared DSFGs at 870  $\mu\text{m}$  (with flux densities measured from the ALMA maps and thus not affected by source confusion) derived in this work is in reasonable agreement with models of galaxy evolution, whereas there have been reports of conflicts at 500  $\mu\text{m}$  (where flux densities are derived from SPIRE). Ultrared DSFGs have a variety of morphologies (from relatively extended disks with smooth radial profiles, to compact sources, both isolated and interacting) and an average size,  $\theta_{\text{FWHM}}$ , of  $1.46 \pm 0.41$  kpc, considerably smaller than the values reported in previous work for less-luminous DSFGs at lower redshifts. The size and the estimated gas-depletion times of our sources are compatible with their being the progenitors of the most massive, compact, red-and-dead galaxies at  $z \sim 2-3$ , and ultimately of local ultra-massive elliptical galaxies or massive galaxy clusters. We are witnessing the birth of the high-mass tail of the red sequence of galaxies.

*Subject headings:* galaxy evolution; sub-mm galaxies; dust emission; number counts

## 1. INTRODUCTION

It has been well known for over fifty years (e.g. Rood 1969) that galaxies with quiescent stellar populations in the local Universe are located in a region of the color-magnitude or color-mass diagram known as the ‘red sequence’ (Bower et al. 1992b,a; Strateva et al. 2001; Blanton et al. 2003; Baldry et al. 2004). Later work suggested that the red sequence was already in place at  $z \gtrsim 2$  (Labbé et al. 2005; Williams et al. 2009; Brammer et al. 2009), possibly as early as  $z \sim 3$  (Whitaker et al. 2011; Nayyeri et al. 2014). The analysis of the stellar populations in so-called ‘red-and-dead’ galaxies at  $z \sim 2-3$  sug-

gests that their formation could have taken place at even earlier times, at  $z \sim 4-6$ , in the form of extreme bursts of star formation (Collins et al. 2009; Thomas et al. 2010; Gobat et al. 2011; Zeimann et al. 2012; Petty et al. 2013).

Until recently, only a handful of dusty star-forming galaxies (DSFGs – e.g. Casey et al. 2014, also sometimes referred to as submm-selected galaxies, SMGs) had been found at  $z \sim 4$  (Capak et al. 2008; Daddi et al. 2009; Coppin et al. 2009; Knudsen et al. 2010; Smolčić et al. 2011; Swinbank et al. 2012). This situation changed quickly following the launch of the *Herschel Space Observatory* (Pilbratt et al. 2010) and its wide-field far-infrared (FIR) surveys, which have enormously increased the number of known DSFGs in the early Universe. This is mainly due

to the selection of very high-redshift DSFGs by looking for sources whose flux densities increase from 250 to 500  $\mu\text{m}$ , as measured by SPIRE (Griffin et al. 2010):  $S_{250} < S_{350} < S_{500}$ , where the various selection criteria employed to date have been described by, for example, Cox et al. (2011); Combes et al. (2012); Dowell et al. (2014); Ivison et al. (2016) and Asboth et al. (2016), but see also §2.

Follow-up spectroscopic observations has confirmed the effectiveness of the ultrared criterion to select DSFGs at  $z = 4\text{--}6$  (e.g. Riechers et al. 2013; Oteo et al. 2016a; Asboth et al. 2016; Riechers et al. 2017; Fudamoto et al. 2017; Zavala et al. 2017). In this work, we present ALMA 870  $\mu\text{m}$  dust continuum observations at  $\sim 0.12''$  resolution (or  $\approx 800$  pc at  $z \sim 4.5$ ) of a sample of 44 ultrared DSFGs at  $z = 4\text{--}6$ , selected from *H-ATLAS* (Eales et al. 2010) and *HerMES* (Oliver et al. 2010), the widest surveys carried out by *Herschel*. The main goals are: 1) to confirm that there exists a significant population of unlensed hyper-luminous DSFGs at  $z = 4\text{--}6$ ; 2) to study the number density of such sources, to inform and constrain galaxy formation and evolution models; and 3) to study their sizes and morphologies, to explore their nature and their likely evolution, hoping to reveal the manner in which the ancestors of today’s most massive galaxies and structures were formed.

This paper is structured as follows: In §2 we present the selection of ultrared DSFGs at  $z \sim 4\text{--}6$ , the sample studied in this work. §3 presents our ALMA high-spatial-resolution observations. The results of the paper are presented and discussed in §4, 5 and 6. Finally, the main conclusions are summarized in §7. The total infrared luminosities ( $L_{\text{IR}}$ ) reported in this work refer to the integrated luminosities between rest-frame 8 and 1000  $\mu\text{m}$ . The reported SFRs are derived from the  $L_{\text{IR}}$  assuming a Salpeter initial mass function (IMF) and the classical Kennicutt (1998) calibration, ignoring for now the possibility of a profoundly different IMF in these objects (see Romano et al. 2017). The sizes and areas are calculated by carrying out 2D elliptical Gaussian fits and using  $A = \pi \times R_1 \times R_2$ , where  $R_1$  and  $R_2$  are the major and minor semi-axes of the best-fit elliptical Gaussians, respectively:  $R_1 = \text{FWHM}_{\text{major}}/2$  and  $R_2 = \text{FWHM}_{\text{minor}}/2$ . We assume a flat Universe with  $(\Omega_m, \Omega_\Lambda, h_0) = (0.3, 0.7, 0.7)$ . For this cosmology, the sky scale is  $\sim 6.6$  kpc/'' at  $z = 4.5$ .

## 2. ULTRARED DSFGS AT $Z > 4$

The dust emission of DSFGs peaks at approximately rest-frame 100–200  $\mu\text{m}$  (Dunne et al. 2000; Farrah et al. 2003; Hwang et al. 2010). As the redshift increases, the dust emission peak shifts to longer wavelengths until at  $z \gtrsim 4$  it is located at or beyond 500  $\mu\text{m}$ . Thus, looking for galaxies whose flux densities rise from 250 to 350  $\mu\text{m}$  and then to 500  $\mu\text{m}$ , it is possible to select DSFGs at  $z > 4$ . These are called ‘500  $\mu\text{m}$  risers’, or ‘ultrared’ DSFGs. At the flux density limits accessible to SPIRE, the number density of these sources is relatively low, meaning that wide-area surveys are needed to select them. The sample of ultrared DSFGs studied in this paper has been taken from Ivison et al. (2016) and Asboth et al. (2016). We refer the reader to those papers for details on the source selection. Briefly, our galaxies were selected

from the *H-ATLAS*<sup>1</sup> Data Release 1 and 2 (Valiante et al. 2016; Bourne et al. 2016, Smith et al. in prep., Maddox et al. in prep., Furlanetto et al. in prep.) and the fourth *HerMES* data release<sup>2</sup>, by looking for galaxies with  $S_{500}/S_{250} \geq 1.5$  and  $S_{500}/S_{350} \geq 1.0$ , where  $S_\lambda$  is the flux density in the SPIRE band centered at  $\lambda$  [ $\mu\text{m}$ ]. The *Herschel* maps for the full sample were then inspected visually by several members of the team to exclude blended sources, and checked for contamination by bright synchrotron emission from radio-loud AGN. With our ultrared criterion, our sample is arguably one of the largest, reddest and most robust available. To put this beyond doubt, we refined our selection criteria still further via 850  $\mu\text{m}$  SCUBA-2 and 870  $\mu\text{m}$  LABOCA imaging, which provide better resolution than SPIRE at 500  $\mu\text{m}$ , to isolate those whose colors are consistent only with  $z > 4$ :  $S_{870}/S_{500} > 0.4$  (e.g. Ivison et al. 2016). Taken together, these criteria ensure the selection of the most secure, ultrared DSFGs.

The validity of the ultrared criterion to select DSFGs at  $z > 4$  has been proven by our recent ALMA and NOEMA spectral scans in the 2 mm and 3 mm windows. These observations aimed to confirm unambiguously the redshifts of our ultrared DSFGs via detection of multiple CO, [C I](1–0) and water emission lines. So far, all spectroscopically confirmed ultrared DSFGs lie at  $z_{\text{spec}} > 3.5$  (Riechers et al. 2013; Asboth et al. 2016; Riechers et al. 2017; Fudamoto et al. 2017). Most sources without spectroscopic confirmation have a single emission line close to the center of the 3 mm band, suggesting  $z > 3$  if the detected lines correspond to CO transitions (lower-redshift options would be in strong disagreement with the FIR-derived photometric redshifts). No lines were detected in the remaining sources, likely due to the lack of depth (see, e.g., the discussion in Fudamoto et al. 2017). For some of our ultrared DSFGs,  $z \sim 6$  is likely, and two sources have indeed been spectroscopically confirmed at  $z \sim 6$  (Riechers et al. 2013; Fudamoto et al. 2017; Zavala et al. 2017).

A subsample of 44 equatorial and southern sources from our full sample of ultrared DSFGs at  $z \sim 4\text{--}6$  selected from *H-ATLAS* and *HerMES* (see Table 1) were chosen for ALMA 870  $\mu\text{m}$  follow-up observations at high spatial resolution ( $\sim 0.12''$  or  $\approx 800$  pc, see §3). These observations constitute the main dataset that we present and analyze in this paper. We note that not all the sources in our sample of ultrared DSFGs were observed with ALMA. Instead, the observations were limited to: 1) sources visible during the required ALMA configuration; 2) sources that could share calibration, to minimize calibration overheads. This is the reason why, for example, no sources from the GAMA-12 or GAMA-15 *H-ATLAS* fields were observed. Table 1 shows the properties of the sample of ultrared DSFGs studied in this paper.

## 3. ALMA HIGH-RESOLUTION IMAGING AT 870 $\mu\text{m}$

Our sample of 44 ultrared DSFGs at  $z \sim 4\text{--}6$  was observed between 2015 June and 2017 May when ALMA was in a relatively extended configuration. Between 37 and 43 antennas were used, with distances from the

<sup>1</sup> <https://www.h-atlas.org>

<sup>2</sup> <http://hedam.oamp.fr/HerMES>

TABLE 1  
 PROPERTIES OF OUR SAMPLE OF ULTRARED DSFGs.

IAU name	Nickname	$z^{(a)}$	$S_{250}$ [mJy]	$S_{350}$ [mJy]	$S_{500}$ [mJy]	$S_{870}$ [mJy]	$S_{870}^{\text{ALMA}^{(g)}}$ [mJy]	SFR [ $M_{\odot} \text{ yr}^{-1}$ ]	$N^{(j)}$
HerMES J003929.5+002424	(RARE) HeLMS_36		140 ± 7	152 ± 8	162 ± 9	50 ± 4	58.5 ± 0.6	~ 7855/ $\mu$	1
HerMES J003814.0-002253	(RARE) HeLMS_38		73 ± 7	119 ± 8	123 ± 9	56 ± 4	48.6 ± 3.4	~ 6526/ $\mu$	1
HerMES J004532.5-000124	(RARE) HeLMS_54		48 ± 7	88 ± 8	97 ± 9	36 ± 4	47.7 ± 0.9	~ 6405	5
HerMES J002220.8-015521	HELMS_RED_4	5.161 <sup>(b)</sup>	62 ± 6	104 ± 6	116 ± 7	41 ± 3	40.9 ± 2.8	~ 5774/ $\mu$	1
HerMES J000303.9+024113	(RARE) HeLMS_42		34 ± 5	54 ± 5	87 ± 5	35 ± 5	42.7 ± 0.9	~ 5734/ $\mu$ <sup>(h)</sup>	2
HATLAS J090045.4+004125	G09-83808	6.027 <sup>(c)</sup>	10 ± 5	25 ± 5	44 ± 6	36 ± 3	36.5 ± 2.1	~ 5635/ $\mu$	1
HATLAS J000124.9-354212	SGP-28124	3.93 <sup>+0.08</sup> <sub>-0.45</sub>	62 ± 8	89 ± 8	118 ± 9	47 ± 6	41.5 ± 1.3	~ 5573/ $\mu$	1
HATLAS J000607.6-322639	SGP-261206	4.242 <sup>(c)</sup>	23 ± 5	45 ± 6	59 ± 7	57 ± 9	40.1 ± 1.5	~ 5371/ $\mu$	1
HATLAS J000624.3-323019	SGP-93302	3.91 <sup>+0.27</sup> <sub>-0.22</sub>	31 ± 4	61 ± 5	62 ± 6	37 ± 4	39.1 ± 3.2	~ 5250/ $\mu$ <sup>(i)</sup>	2
HATLAS J000306.9-330248	SGP-196076	4.425 <sup>(d)</sup>	29 ± 5	29 ± 6	46 ± 7	33 ± 4	34.6 ± 2.3	~ 4643	3
HerMES J000727.1+015626	HELMS_RED_19		53 ± 5	72 ± 5	82 ± 5	34 ± 5	33.3 ± 2.2	~ 4471/ $\mu$	1
HerMES J003257.1-424736	ELAISS1_7		48 ± 4	69 ± 5	71 ± 5	—	32.9 ± 1.2	~ 4418/ $\mu$	1
HerMES J000900.6+050709	HELMS_RED_69		37 ± 5	43 ± 5	70 ± 5	42 ± 5	30.1 ± 1.4	~ 4042/ $\mu$ <sup>(h)</sup>	1
HerMES J003943.5-003955	HELMS_RED_118		32 ± 6	57 ± 6	74 ± 7	26 ± 4	29.9 ± 2.1	~ 4015/ $\mu$	1
HerMES J043657.5-543809	ADFS_27	5.655 <sup>(e)</sup>	15 ± 5	19 ± 6	24 ± 3	25 ± 2	26.8 ± 1.0	~ 3968	2
HerMES J022656.6-032709	XMM_30		30 ± 5	50 ± 8	55 ± 7	28 ± 2	27.8 ± 2.4	~ 3933/ $\mu$	1
HATLAS J084937.0+001455	G09-81106	4.53 <sup>(c)</sup>	14 ± 5	31 ± 6	48 ± 7	30 ± 5	28.4 ± 0.8	~ 3840/ $\mu$	1
HATLAS J225432.0-323904	SGP-317726	3.69 <sup>+0.39</sup> <sub>-0.30</sub>	20 ± 5	35.1 ± 5	40 ± 6	19 ± 3	26.9 ± 2.9	~ 3612	1
HATLAS J004223.5-334340	SGP-354388	4.002 <sup>(f)</sup>	17 ± 6	40 ± 7	54 ± 8	64 ± 11	24.1 ± 1.7	~ 3257	3
HerMES J235808.7+005557	HELMS_RED_68		55 ± 5	74 ± 6	76 ± 7	27 ± 7	24.1 ± 3.1	~ 3236	2
HerMES J002737.3-020759	HELMS_RED_31	3.798 <sup>(b)</sup>	36 ± 7	49 ± 6	72 ± 7	23 ± 4	22.9 ± 4.1	~ 3092/ $\mu$	1
HerMES J043913.5-542546	ADFS_17		23 ± 6	48 ± 7	52 ± 8	—	21.1 ± 0.8	~ 2833	3
HATLAS J084059.3-000417	G09-81271	4.62 <sup>+0.46</sup> <sub>-0.38</sub>	15 ± 5	31 ± 6	42 ± 7	30 ± 4	20.5 ± 0.7	~ 2753/ $\mu$	1
HerMES J004724.7+010114	HELMS_RED_82		47 ± 7	76 ± 8	76 ± 9	27 ± 4	19.6 ± 2.3	~ 2632/ $\mu$	1
HerMES J002851.4-431351	ELAISS1_18		26 ± 4	43 ± 5	45 ± 5	27 ± 3	18.2 ± 0.8	~ 2444	2
HerMES J002314.7+001243	HeLMS_182		33 ± 5	58 ± 7	73 ± 6	31 ± 4	17.7 ± 0.7	~ 2377	1
HATLAS J000018.0-333737	SGP-72464	3.06 <sup>+0.21</sup> <sub>-0.19</sub>	20 ± 6	30 ± 8	38 ± 8	10 ± 4	16.9 ± 0.4	~ 2269	1
HerMES J021914.2-043740	XMM_76		26 ± 5	37 ± 8	38 ± 6	17 ± 2	16.8 ± 1.6	~ 2256/ $\mu$	1
HerMES J044509.9-530006	ADFS_31		19 ± 7	34 ± 7	40 ± 7	25 ± 5	16.7 ± 0.8	~ 2242	2
HerMES J235830.9-005632	HELMS_RED_270		48 ± 5	62 ± 5	64 ± 5	29 ± 5	16.5 ± 0.9	~ 2216	2
HATLAS J010740.9-22709	SGP-32338	3.93 <sup>+0.26</sup> <sub>-0.24</sub>	16 ± 7	33 ± 8	64 ± 8	23 ± 3	16.4 ± 0.9	~ 2202	2
HerMES J002933.9-421212	ELAISS1_40		25 ± 4	34 ± 2	41 ± 5	—	14.4 ± 0.6	~ 1934	1
HATLAS J225855.7-312405	SGP-499646	4.68 <sup>+0.49</sup> <sub>-0.34</sub>	6 ± 6	10 ± 6	41 ± 7	19 ± 3	14.1 ± 1.6	~ 1893	1
HATLAS J001223.5-313242	SGP-213813	3.47 <sup>+0.40</sup> <sub>-0.32</sub>	24 ± 6	35 ± 8	36 ± 8	18 ± 4	13.9 ± 0.7	~ 1866	1
HerMES J003352.2-452010	ELAISS1_26		22 ± 4	34 ± 5	38 ± 5	—	13.5 ± 0.6	~ 1812	1
HATLAS J083909.9+022718	G09-79552	3.59 <sup>+0.34</sup> <sub>-0.26</sub>	17 ± 6	38 ± 8	43 ± 9	17 ± 4	12.7 ± 0.6	~ 1705	1
HATLAS J084113.6-004114	G09-59393	3.70 <sup>+0.35</sup> <sub>-0.26</sub>	24 ± 7	44 ± 8	47 ± 9	24 ± 4	12.4 ± 0.4	~ 1665	2
HATLAS J222919.2-293731	SGP-385891	3.70 <sup>+0.29</sup> <sub>-0.24</sub>	13 ± 8	46 ± 10	60 ± 11	21 ± 4	11.1 ± 0.7	~ 1490	2
HATLAS J003131.1-293122	SGP-392029	3.42 <sup>+0.47</sup> <sub>-0.32</sub>	18 ± 7	31 ± 8	35 ± 8	14 ± 4	10.8 ± 0.8	~ 1450	2
HATLAS J085156.0+020533	G09-80658	4.07 <sup>+0.09</sup> <sub>-0.72</sub>	18 ± 6	32 ± 8	40 ± 9	18 ± 4	10.7 ± 0.7	~ 1437	2
HerMES J021743.9-030914	XMM_15		25 ± 5	39 ± 8	47 ± 7	19 ± 3	9.4 ± 0.5	~ 1262	1
HATLAS J084659.0-004219	G09-80620	4.01 <sup>+0.22</sup> <sub>-0.78</sub>	14 ± 5	25 ± 7	28 ± 8	13 ± 4	8.4 ± 0.7	~ 1128	2
HATLAS J231146.6-313518	SGP-386447	4.89 <sup>+0.78</sup> <sub>-0.73</sub>	11 ± 6	34 ± 6	34 ± 7	34 ± 8	6.5 ± 0.6	~ 873	1
HATLAS J001526.4-353738	SGP-135338	3.06 <sup>+0.33</sup> <sub>-0.26</sub>	33 ± 7	44 ± 8	53 ± 9	15 ± 4	6.1 ± 0.4	~ 819	1

<sup>a</sup>Redshifts with error bars are photometric redshifts derived from *Herschel*+LABOCA/SCUBA-2 photometry, from Ivison et al. (2016). Redshifts without error bars are unambiguous spectroscopic redshifts, taken from different works (see below).

<sup>b</sup>From Asboth et al. (2016)

<sup>c</sup>From Fudamoto et al. (2017)

<sup>d</sup>From Oteo et al. (2016a)

<sup>e</sup>From Riechers et al. (2017).

<sup>f</sup>From Oteo et al. (2017a).

<sup>g</sup>Flux densities obtained from the primary-beam corrected, tapered ALMA maps at  $\sim 0.8''$  resolution.

<sup>h</sup>No clear signatures of lensed features are seen in these ALMA high-resolution images, but the proximity to a near-IR source could indicate weak gravitational magnification.

<sup>i</sup>Source with both lensed and unlensed components.

<sup>j</sup>Number of components our ultrared DSFGs are resolved into.

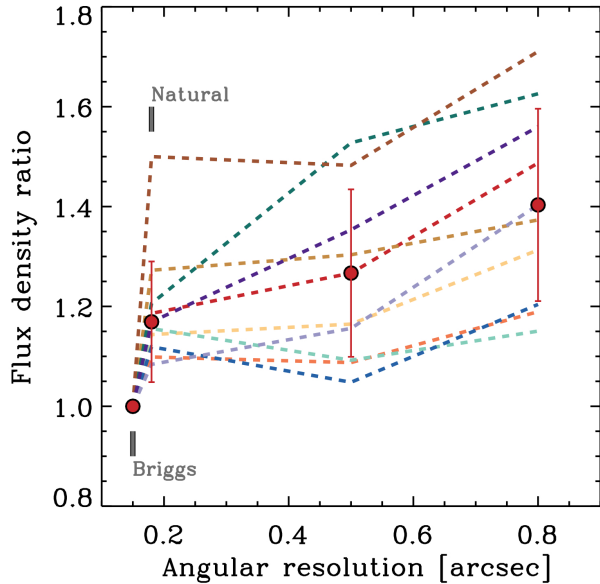


FIG. 1.— Flux density ratio for several of our unlensed ultrared DSFGs, for four different weighting schemes and  $uv$  tapers (in order of increasing beam size): 1) Briggs weighting with `robust` = 0.5, 2) natural weighting, 3) natural weighting and  $\sim 0.5''$  tapering, and 4) natural weighting and  $\sim 0.8''$  tapering. The flux density ratios are measured with respect to Briggs weighting with `robust`=0.5. The trend for individual sources is shown by the dashed curves, while red dots represent the average. In most cases we see that natural weighting recovers a significant fraction of the flux recovered when tapering to  $\sim 0.8''$ .

center of the array of up to 1.6 km. The raw data were calibrated using the ALMA pipeline, then the calibrated visibilities were imaged using Briggs weighting with `robust` = 0.5, giving an average beam size of  $0.12''$ , or  $\approx 800$  pc for an unlensed source at  $z = 4.5$ . The continuum r.m.s. sensitivity reached an average of  $0.1 \text{ mJy beam}^{-1}$ . Later on in the paper, we will refer to these as the ‘full-resolution maps’, although slightly higher resolution would be achieved using uniform weighting which highlights more compact scales than Briggs with `robust` = 0.5. We will also study the influence of different  $uv$  weighting schemes on the recovered flux density, morphology and size of our sources, for which several `ROBUST` values will be considered along with uniform and natural weightings (the latter recovers more extended scales than Briggs weighting with `robust` = 0.5), and natural weighting with a Gaussian taper.

At the frequency of our observations, the FWHM of the ALMA primary beam is about  $17''$  or 112 kpc at  $z = 4.5$ . Due to this relatively small field of view (FoV), it is plausible that we could fail to detect one or more companions to our ultrared DSFGs, especially for those sources where the LABOCA/SCUBA-2 emission appears extended. We will go back to this issue in §3.1.

### 3.1. Measuring flux densities

The high-spatial resolution of our ALMA observations ( $\sim 0.12''$  FWHM) could mean that some of the  $870 \mu\text{m}$  flux density of our ultrared DSFGs is missed during imaging. In this section, we explore how the recovered flux densities of our ultrared DSFGs vary as a function of the

weighting schemes and  $uv$  tapering used during imaging. To accomplish this we also image the calibrated visibilities using natural weighting and natural weighting with two  $uv$  tapers, giving two spatial resolutions:  $\sim 0.5''$  and  $\sim 0.8''$ .

We show in Fig. 1 the Briggs-to-natural flux density ratio (measured using the CASA task `IMFIT` in the primary-beam corrected maps) of some of our ultrared DSFGs, randomly selected from the full sample (we do not include all sources in Fig. 1 for the sake of clarity) as a function of the beam size of the maps. All flux densities have been normalized to the flux density of the sources in the maps produced with Briggs weighting and `ROBUST` = 0.5. We see in Fig. 1 that the recovered flux densities increase with the beam size, as expected. On average, natural weighting recovers most ( $\sim 85\%$ ) of the flux density of our galaxies, assuming that the flux densities provided by the tapered maps at  $\sim 0.8''$  resolution represent the true total flux (this is motivated by the fact that most sources are unresolved in the tapered maps at  $\sim 0.8''$  resolution). On the other hand, the Briggs weighting misses  $\sim 30\%$  of the total flux density. These results are in agreement with Hodge et al. (2016) for a sample of luminous, lower-redshift DSFGs observed at similar angular resolution. We note that while tapering to  $\sim 0.8''$  resolution recovers most of the flux density of our sources, the angular resolution is then too poor to determine meaningful sizes.

We show in Table 1 the primary-beam corrected flux density of our sources at  $870 \mu\text{m}$ , obtained from tapered maps at  $0.8''$  resolution. The ALMA flux density at  $870 \mu\text{m}$  of the sources whose emission is resolved into several sub-components corresponds to the sum of the flux densities of all sub-components. The ALMA flux densities quoted in Table 1 are measured at a similar frequency to the LABOCA/SCUBA-2 observations presented in Ivison et al. (2016). However, we see significant flux density differences between single-dish and ALMA observations in some of the sources. One of the most obvious cases is SGP-354388, for which LABOCA measured  $S_{870} = 64 \pm 11 \text{ mJy}$  while the ALMA-derived flux density is  $S_{B70} = 24.1 \pm 1.7 \text{ mJy}$ . For this source, ultra-deep ALMA 2 mm observations reveal at least 10 DSFGs distributed over a  $\sim 40''$  wide region (Oteo et al. 2017a). While all these components are contributing to the LABOCA flux density (and the LABOCA emission appears extended due to the superposition of the  $870 \mu\text{m}$  emission of all these sources), only one of them (the brightest at 2 mm) is covered by the ALMA FoV at  $870 \mu\text{m}$ . This suggests that some of the flux density losses in the ALMA maps might be due to multiple components lying outside of the ALMA band 7 FoV. There are also deep 3 mm observations for SGP-196076, SGP-32338, ADSF 27, HELMS\_RED.4, and HELMS\_RED.31, and in all these cases the deep 3 mm maps reveal that all sub-components contributing to the SCUBA-2/LABOCA flux density are within the ALMA band 7 primary beam. For these sources, the SCUBA-2/LABOCA and ALMA flux densities are in good agreement, within the uncertainties. Due to the lack of 3 mm imaging for most of the sources, we cannot explore further whether the differences in the flux densities between single-dish and ALMA observations are due to sources located outside of the ALMA FoV, but the few existing data do point



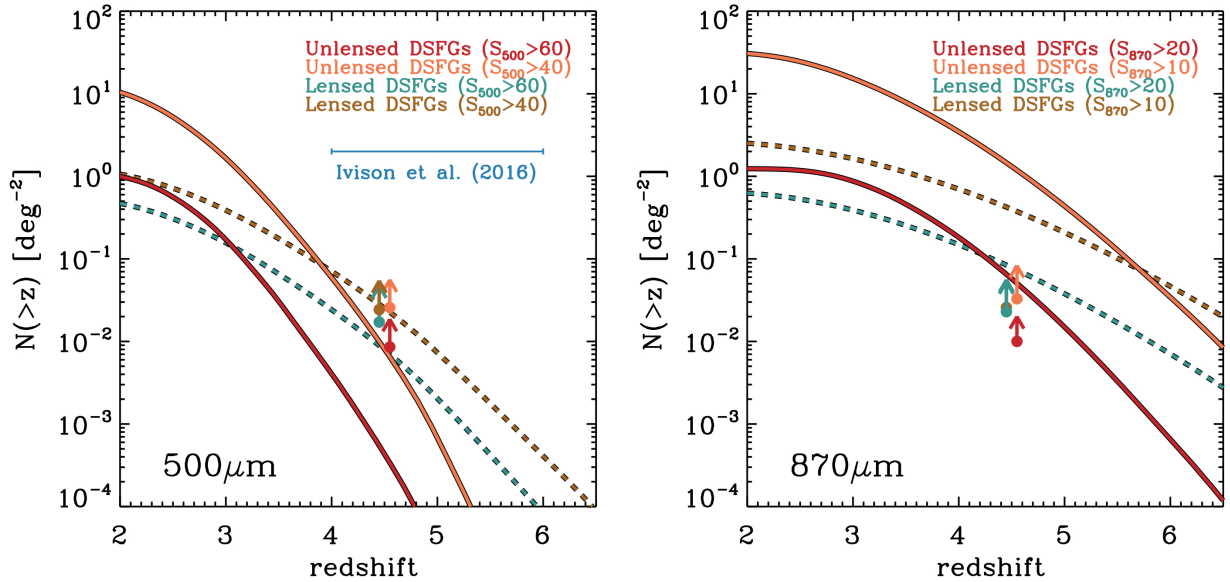


FIG. 2.— Expected number of lensed and unlensed DSFGs with  $S_{500} > 40$  mJy and  $S_{500} > 60$  mJy (*left*) and  $S_{870} > 20$  mJy and  $S_{870} > 10$  mJy (where the flux densities have been obtained from the ALMA tapered maps at  $0.8''$  resolution – *right*) as a function of redshift according to the Cai et al. (2013) models. We consider here that the average redshift of the sample is  $z = 4.5$ . For the lensed DSFGs we have considered a maximum amplification factor of  $\mu_{\max} = 15$  (Negrello et al. 2017). The vertical arrows represent lower limits found in our work. Recall that only lower limits can be provided in this work because we study only the ultrared DSFGs observed with ALMA, not the full sample. The arrows for lensed sources have been shifted to  $z = 4.45$  and those for unlensed sources to  $z = 4.55$ , for clarity. For reference, we include the number counts for the full sample of ultrared DSFGs in *H*-ATLAS taken from (Ivison et al. 2016). We see that models cannot reproduce the number of unlensed DSFGs at  $500 \mu\text{m}$  in any of the two flux density ranges considered. The model counts underestimation for unlensed sources is more significant at higher flux densities. The agreement with lensed sources is better, mostly in the flux density range  $S_{500} > 40$  mJy, although it may be that the ‘true’ number counts are much higher than the lower limits given here. At  $870 \mu\text{m}$  we see that models might be able to reproduce the number of sources in our sample, although it is difficult to say how stringent our lower limits are. In any case, we see a strong difference between the number counts at  $500 \mu\text{m}$  (measured from SPIRE) and at  $870 \mu\text{m}$  (measured from ALMA, after refinement with SCUBA-2 and LABOCA). Possible reasons for this difference include flux boosting in SPIRE  $500 \mu\text{m}$ , which might affect the flux densities by tens of %, or clustering in the SPIRE bands due to the large SPIRE beam. At the redshift of our ultrared DSFGs ( $z = 4\text{--}6$ ) the models predict that a significant fraction of ultrared DSFGs are expected to be lensed, in agreement with our results.

in that direction. We note that the SFRs quoted in Table 1 have been obtained from the ALMA data (see §4 for details), so if there are sources out of the ALMA FoV which contribute to the SPIRE flux densities and are at the same redshift, the SFRs of our targets would be even higher. The small FoV of our ALMA observations cannot explain those cases where the ALMA flux densities are higher than the LABOCA ones. Examples include (RARE) HeLMS\_54 or (RARE) HeLMS\_42, which are among the brightest sources in our sample. We have excluded the possibility that emission lines are contributing to the narrower ALMA band (Smail et al. 2011).

#### 4. THE MOST LUMINOUS STARBURSTS IN THE EARLY UNIVERSE

The modest depth of the wide-field *H*-ATLAS and *Her*MES surveys means that our ultrared criterion selects among the brightest sources ever found at  $z \sim 4\text{--}6$ . Any sources confirmed to be unlensed would be the among the most luminous starbursts in the early Universe (some examples are shown in Fig. 3). All unlensed DSFGs spectroscopically confirmed to lie at  $z_{\text{spec}} > 4$  so far had  $\text{SFR} \lesssim 3,000 M_{\odot} \text{yr}^{-1}$ , including GN20 at  $z_{\text{spec}} \sim 4.1$  (Hodge et al. 2012), ALESS 73.1 at  $z_{\text{spec}} \sim 4.76$  (Coppin et al. 2009), AzTEC-1 at  $z_{\text{spec}} \sim 4.3$  (Yun et al. 2015), Vd-17871 at  $z_{\text{spec}} = 4.622$  (Smolčić et al. 2015), or AzTEC-3 at  $z_{\text{spec}} \sim 5.3$  (Riechers et al. 2014). Table 1 lists the total SFRs of all the sources in our sample.

These have been derived from their total IR luminosity, obtained by re-scaling the ALESS template (Swinbank et al. 2014) to their observed ALMA  $870 \mu\text{m}$  flux densities (in the tapered maps at  $\sim 0.8''$  resolution, see §3.1). We have used this method instead of fitting to the *Herschel* and LABOCA/SCUBA-2 photometry because the latter is more likely to be affected by confusion and by sources which outside of the ALMA FoV at  $870 \mu\text{m}$ . This is justified because the ALESS template has been shown to provide a good representation of the FIR spectral energy distribution (SED) for most  $z = 4\text{--}6$  ultrared DSFGs (Ivison et al. 2016). We have used spectroscopic redshifts if available; otherwise, we have assumed the average photometric redshift of the sample  $z \sim 4.5$ .

Using a fixed template to estimate the total SFRs of our galaxies adds an uncertainty. For a source with  $S_{870} = 20$  mJy at  $z = 4$ , the ALESS template (the one used in our work to measure SFRs) gives  $\text{SFR} \sim 2,700 M_{\odot} \text{yr}^{-1}$ . Among the templates used in Ivison et al. (2016), which include a representative range of FIR SEDs, only the Cosmic Eyelash (Swinbank et al. 2010; Ivison et al. 2010) and Pearson et al. (2013) templates give slightly lower SFRs:  $\text{SFR} \sim 2,300$  and  $\sim 1,950 M_{\odot} \text{yr}^{-1}$ , respectively. The template associated with Arp 220 and the one reported by Pope et al. (2008) give higher SFRs,  $\text{SFR} \sim 4,900$  and  $\sim 3,000 M_{\odot} \text{yr}^{-1}$ , respectively. The same happens for the templates as-

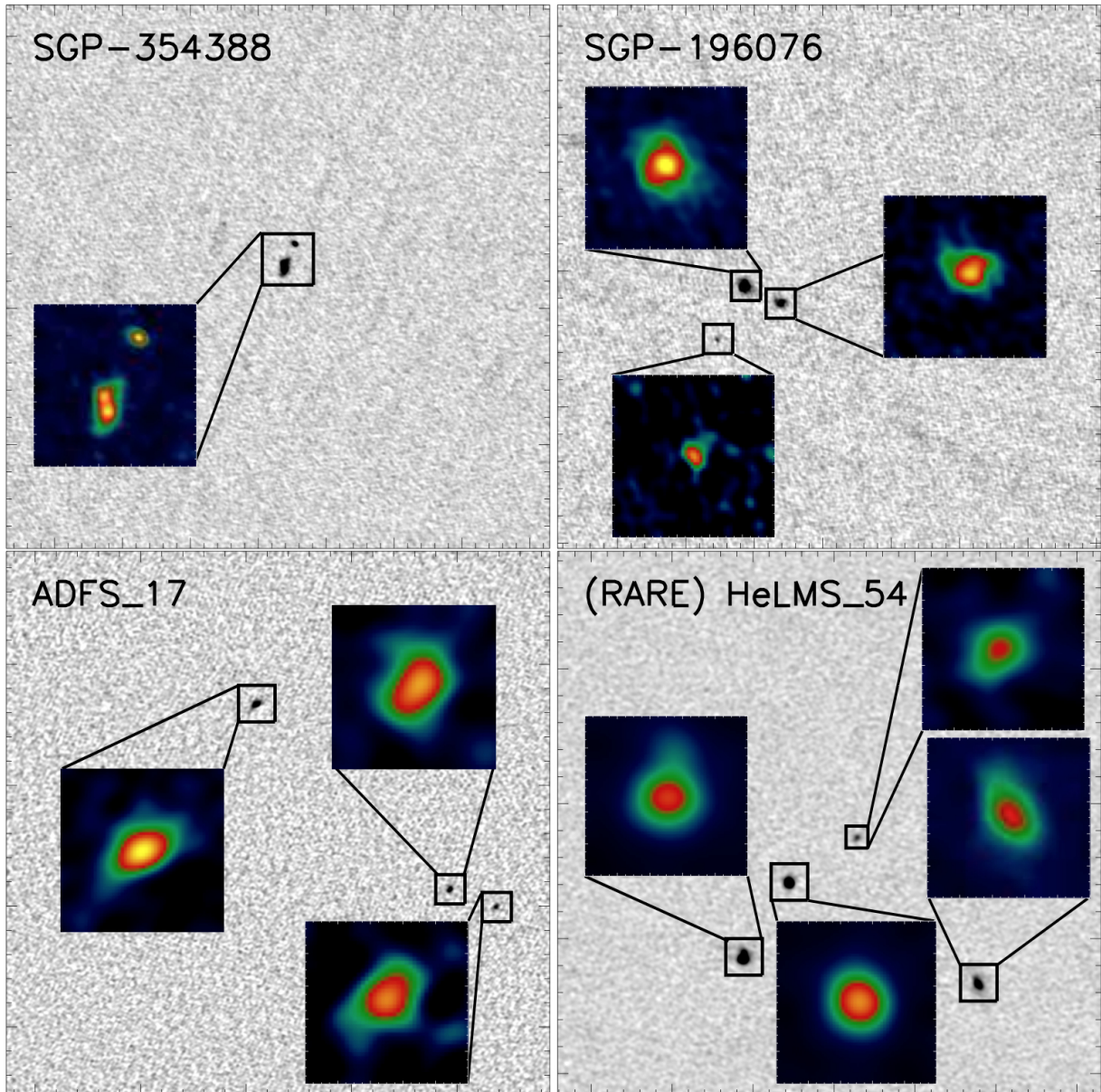


FIG. 3.— ALMA  $870\ \mu\text{m}$  dust continuum imaging at  $\sim 0.12''$  (or  $\approx 800\ \text{pc}$ ) spatial resolution for four of our brightest ultrared DSFGs. For clarity, the images shown here have not been corrected for the primary beam response. The images are  $30''$  on each side and thus cover an area larger than the primary beam. Zoomed images are included to show the morphologies of the different sub-components into which our ultrared DSFGs are resolved. Images of the full sample are included in the Appendix. We see a wide range of morphologies, from relatively extended interacting disks (e.g. SGP-196076 – Oteo et al. 2016a) to compact starbursts (SGP-354388) or sources split into up to five components, such as (RARE) HeLMS\_54 (note that the faintest component is not shown in zoom, due to lack of space).

sociated with the lensed source G15.141 at  $z = 4.24$  (Lapi et al. 2011; Cox et al. 2011), which gives SFR  $\sim 4,450\ M_{\odot}\ \text{yr}^{-1}$ . Although the uncertainties can be significant, we are therefore being conservative: the SFRs of our galaxies are not artificially high because of the chosen template but instead because they are genuinely extremely luminous.

The most luminous galaxy in our sample is (RARE) HeLMS\_54, with a total SFR of  $\sim 6,400\ M_{\odot}\ \text{yr}^{-1}$ , but there are several other extreme, hyper-luminous starbursts, such as SGP-196076 (already studied in depth by Oteo et al. 2016a), SGP-317726, ADFS\_27 (Riechers et al. 2017) and HeLMS\_RED\_68.

#### 4.1. Comparison with models

Fig. 2 shows model predictions for the number of unlensed DSFGs as a function of redshift at 500 and  $870\ \mu\text{m}$ . In each case, two flux density ranges are considered with the aim of comparing the brightest sources and the full sample:  $S_{500} > 60\ \text{mJy}$  and  $S_{500} > 40\ \text{mJy}$  for the 500  $\mu\text{m}$  flux densities and  $S_{870} > 20\ \text{mJy}$  and  $S_{870} > 10\ \text{mJy}$  for the 870  $\mu\text{m}$  flux densities (the latter measured from the ALMA maps, tapered to  $\sim 0.8''$  resolution). The associated number counts are  $N(S_{500} > 60\ \text{mJy}) > 8.6 \times 10^{-3}\ \text{deg}^{-2}$ ,  $N(S_{500} > 40\ \text{mJy}) > 25.7 \times 10^{-3}\ \text{deg}^{-2}$ ,  $N(S_{870} > 20\ \text{mJy}) > 10.0 \times 10^{-3}\ \text{deg}^{-2}$  and  $N(S_{870} > 10\ \text{mJy}) > 32.9 \times 10^{-3}\ \text{deg}^{-2}$ . We highlight that in this work we can only provide lower limits on the number

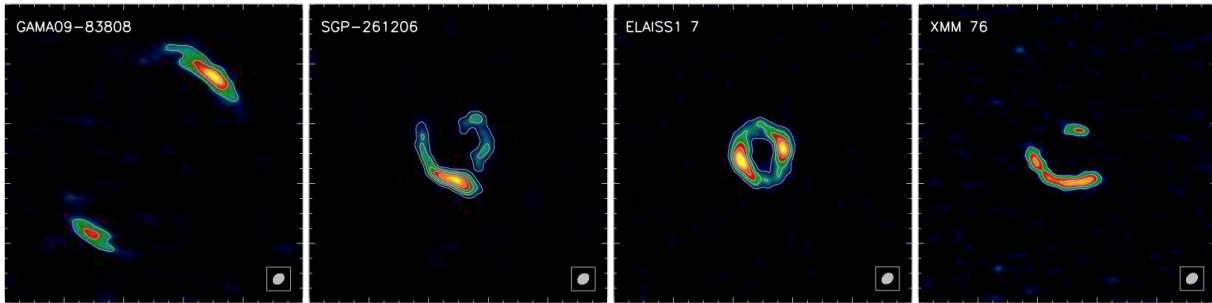


FIG. 4.— ALMA  $870\ \mu\text{m}$  dust continuum imaging of some of our lensed ultrared DSFGs at  $z \sim 4-6$ . All images are  $4''$  on each side. Grey contours represent the dust continuum emission, from  $5\sigma$  in steps of  $5\sigma$ . We expect FIR-bright sources in our sample to be lensed (see Negrello et al. 2010, and Fig. 2) but we see here that some fainter galaxies are also lensed, such as XMM76. From now on we will not consider lensed sources, since studying the morphology and size requires lens modeling that increases the uncertainties of our results. Detailed analysis of the lensed sources will be presented elsewhere.

counts because not all ultrared DSFGs in our initial *Herschel* sample have been observed by ALMA. The galaxy evolution models have been taken from Cai et al. (2013) (see also Negrello et al. 2017). These models reproduce the SCUBA and ALMA  $850\ \mu\text{m}$  number counts at the faint end fairly well (Oteo et al. 2016b; Knudsen et al. 2008) and also the SCUBA number counts (Coppin et al. 2006) at the bright end (it slightly over-predicts the latest SCUBA-2 number counts from Geach et al. 2017 at the bright end). The small disagreement with observations might be due to the fact that these models adopt a single, representative FIR SED (resembling that of the Cosmic Eyelash), and dust temperature and dust emissivity variations affect the number counts at FIR, submm and mm wavelengths.

The Cai et al. (2013) models at  $500\ \mu\text{m}$  are not able to predict the number of unlensed ultrared DSFGs that we see in our sample, in either of the flux density ranges considered. The models underestimation is more significant at higher flux density levels, where our sources are about  $10\times$  more abundant than predicted. In principle, this might suggest that revision should be applied to models so that they can reproduce the number of observed sources. However, the disagreement is less evident when comparing with the number counts at  $870\ \mu\text{m}$ . In the right panel of Fig. 2 we see that the lower limits are still compatible with the models, although it is difficult to assess how stringent the lower limits really are. In any case, it is evident that there is a significant difference when comparing our number of sources with models at  $500\ \mu\text{m}$  (where the flux densities have been obtained from SPIRE observations) and at  $870\ \mu\text{m}$  (where the flux densities have been obtained from our ALMA observations).

How can we explain the differences between  $500$  and  $870\ \mu\text{m}$ ? First, our SPIRE flux densities have not been corrected for flux boosting. As discussed in Ivison et al. (2016), this is because the correction factor is more uncertain than the correction itself. This lack of correction means that the SPIRE flux densities are likely overestimated by tens of % in some sources. Another issue potentially affecting the SPIRE flux densities is source clustering, due to the relatively large SPIRE beam, especially at  $500\ \mu\text{m}$  where flux densities could be contaminated by FIR emission from other IR-bright sources, close by. These effects have clearly not affected the ultrared selection technique responsible for selecting our sam-

ple, since most sources in our sample with spectroscopic redshifts have been confirmed to lie at  $z_{\text{spec}} \sim 4-6$ . This is likely because of the very significant sample refinement that was possible by imaging the ultrared DSFG candidates at higher spatial resolution and at longer wavelengths with SCUBA-2 and LABOCA (see Ivison et al. 2016).

The ALMA flux densities are not affected by either of these issues (although they might be under-estimated due to the relatively small FoV in band 7). We therefore argue that the number counts at  $870\ \mu\text{m}$  are a more reliable observable to compare with models. In this way, the tension between models and observations might not be as significant as previously thought (Asboth et al. 2016). In order to more robustly test the models we require ALMA high-resolution observations of the full sample of ultrared DSFGs, preferably with small mosaics to cover more area, and we also need unambiguous spectroscopic redshifts to confirm that our ultrared DSFGs lie at  $z \sim 4-6$  and to confirm that the multiple sub-components into which our ultrared DSFGs are typically resolved are all at the same redshift and thus belong to the same star-bursting group.

## 5. LENSED ULTRARED DSFGS AT $Z \sim 4-6$

The spatial resolution of our ALMA observations allows us to identify the lensed ultrared DSFGs in our sample by looking for signatures of lensed emission such as elongations, arcs and rings. The high-resolution images of some lensed ultrared DSFGs in our sample are presented in Fig. 4 (the full sample is shown in Figures 8, 9, 10, and 11, except XMM.30 and HeLMS\_RED.4, which will be presented in a forthcoming paper) where lensing signatures are evident in all the sources. In addition to the lensing features, we have also explored possible lensing effects by using the available deep near-IR imaging in our fields: if there is a relatively small offset ( $\lesssim 1.5 - 2''$ ) between the ALMA position of an ultrared DSFG and a near-IR source, then the ultrared DSFG is likely lensed by the near-IR source, which would likely lie at lower redshift than the ultrared DSFG. Doing this, we realized that even though there is no clear evidence of lensed signatures in the images of (RARE) HeLMS\_42 and HeLMS\_RED.69, their proximity to a near-IR source may well indicate weak gravitational magnification (see, e.g., galaxy T in Ivison et al. 2013). As noted by Fu-



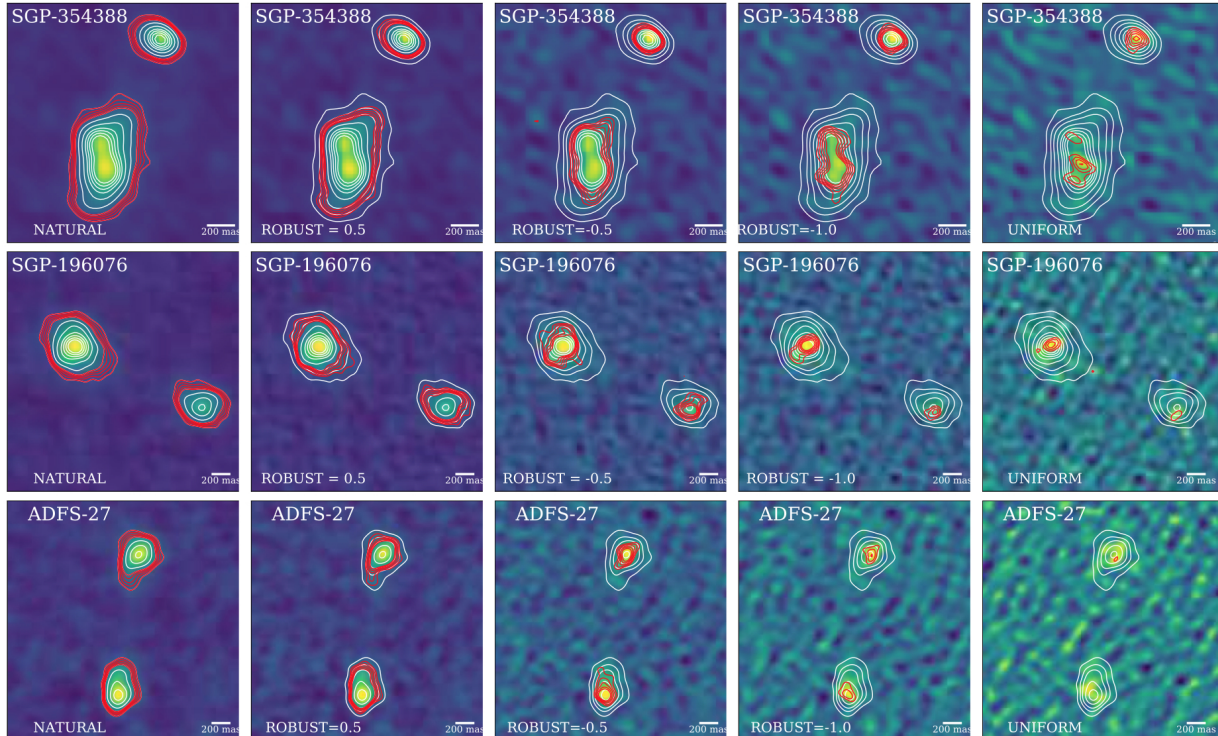


FIG. 5.— Three of our brightest ultrared DSFGs – each row corresponds to one source – imaged using different weighting schemes. From left to right: natural, Briggs with different values of the robust parameter, and uniform. These reveal their extended and compact emission to different degrees. Natural weighing recovers more extended emission, while uniform weighting highlights the most compact emission. Therefore, on each row, from left to right, we see from the most extended to the most compact features. On each row, white contours (starting from  $4\sigma$ , in steps of  $4\sigma$ ) represent the emission in the map obtained with natural weighting. Red contours (from 4 to  $8\sigma$  in steps of  $1\sigma$ ) represent the emission in each individual map. We see that when using uniform weighting (which highlights the most compact emission) most of the emission disappears, confirming that a significant fraction of the dust emission in our ultrared DSFGs is extended relative to the ALMA synthesized beam used here.

damoto et al. (2017), the lack of a near-IR counterpart at the depth of, for example, the VIKING survey (Edge et al. 2013), which is the deepest available in some of our fields, does not guarantee that a source is unlensed. DSFGs gravitationally amplified by a galaxy cluster sometimes lack clear foreground counterparts (e.g. Nayyeri et al. 2017).

We find 18 lensed ultrared DSFGs, representing 40% of our ALMA sample. The majority of the lensed sources are in the bright flux density regime, although others are fainter, such as XMM 76.

Fig. 2 shows that models suggest a notable contribution of lensed sources in our flux density and redshift ranges. At  $S_{870} > 20$  mJy, models predict that the number of lensed ultrared DSFGs is higher than the number of unlensed ones, at least at  $z > 4.5$ , while the number of lensed ultrared DSFGs is about  $\sim 2 - 3\times$  lower than the number of unlensed at  $S_{870} > 10$  mJy. Due to the different sources of incompleteness in our sample we cannot derive reliable fractions of lensed sources as a function of redshift or flux density, but we can trivially conclude that the fraction of lensed sources seen in our sample is not surprising according to models.

In this work we aim to measure accurate sizes and morphologies for our ultrared DSFGs. For this reason we will exclude the lensed sources from our analysis, since the need for lens modeling will significantly affect the uncertainties of the results. Detailed analysis of the lensed

sources will be presented elsewhere.

## 6. MORPHOLOGY AND PHYSICAL SCALE OF DUST EMISSION AT $Z > 4$

We analyze in this section the morphologies and the physical scales of the dust emission in our sample of unlensed, ultrared DSFGs at  $z \sim 4-6$ . Note that the morphology of the dust emission in SGP-196076 and ADFS 27 has been already analyzed using data from the ALMA project used in this work, by Oteo et al. (2016a) and Riechers et al. (2017), respectively, but we include these sources here for the sake of completeness.

### 6.1. Morphologies

The fine spatial resolution of our ALMA  $870 \mu\text{m}$  observations allows us to study the morphology of a large sample of DSFGs at  $z \sim 4-6$  in unprecedented detail – see Figs 3, 8, 9, 10, and 11. We see a diverse variety of morphologies: relatively extended smooth, disk-like shapes (SGP-196076); dust emission resolved into several interacting, compact components (SGP-354388); several isolated compact sources (ADFS 17) and single, compact sources (XMM 15). The last column in Table 1 gives the number of components our ultrared DSFGs are resolved into (we consider only  $> 5\sigma$  continuum detections, to avoid spurious sources – Oteo et al. 2016b). The remarkable source multiplicity for HeLMS 23, with its four bright components, is compatible with the findings for the classical SMG population at  $z \sim 2.5$  (Karim et al.

2013; Hodge et al. 2013; Simpson et al. 2015a). These multiple components do not necessarily have to lie at the same redshift and be physically related to each other, but having so many bright, unrelated sources within one ALMA FoV at  $870\ \mu\text{m}$  is unlikely given the most recent ALMA number counts at  $870\ \mu\text{m}$  (Simpson et al. 2015b; Oteo et al. 2016b)

To further explore the presence of extended star formation in some of our ultrared DSFGs we have used different weighting schemes during the imaging and cleaning processes (some results are shown in Fig. 5). We see that when going from natural weighing (which recovers more extended emission) to uniform weighing (which highlights the most compact emission), most of the dust emission in our ultrared DSFGs disappears. For example, when using uniform weighting, the dust emission is barely detected in the two interacting components of SGP-196076 (only the center of the brightest component remains detected) and ADFS 27. Therefore, we conclude that a significant part of the star formation in our sources is extended, and only a few cases show very compact emission, like in the northern component of SGP-354388. This result also suggests that caution should be taken when analyzing the morphology and size of the dust emission in high-redshift DSFGs, since these are dependent on the weighting schemes used to create the interferometric maps (see also §6.2 and Hodge et al. 2016).

There is no obvious trend between the morphology of our ultrared DSFGs and their SFRs. The likely reason is that our sample contains only the most luminous DSFGs at  $z = 4\text{--}6$ ; in order to study such trend, a less luminous control sample would be more informative. Actually, we find ultrared DSFGs which are resolved into multiple components both at our bright (see for example (RARE) HeLMS\_54) and faint end (see for example SGP-392029).

### 6.2. Sizes

Before discussing the sizes of our ultrared DSFGs, we compare measurements obtained with Briggs weighting and  $\text{ROBUST} = 0.5$  and with natural weighting. This is shown in Fig. 6. For each map and for each source, we have measured the size of the different components of our ultrared DSFGs by fitting their dust continuum images with 2D elliptical Gaussian profiles. This has been done with the CASA task, IMFIT, as in previous work (Simpson et al. 2015a). On each map, we first fit the dust emission of the brightest component. Then, we fit the dust emission of the brightest component in the residual map (if any) from the previous fit. This is repeated until there are no remaining detections at  $> 5\sigma$  in the last residual map. It can be seen in Fig. 6 that the measured deconvolved sizes of our ultrared DSFGs is higher in the maps obtained with natural weighting with respect to those in the maps obtained with Briggs weighting and  $\text{ROBUST} = 0.5$ , as expected, by a factor of  $1.12\times$ . The change in size runs in parallel to the change in flux density reported in §3.1. From now on, we report sizes by using the maps obtained with Briggs weighting and  $\text{ROBUST} = 0.5$ , bearing in mind that flux densities are  $1.17\times$  times higher and sizes are  $1.12\times$  times higher in the natural weighted maps.

Table 2 quotes the flux densities (obtained from the primary-beam-corrected maps) and sizes (de-convolved

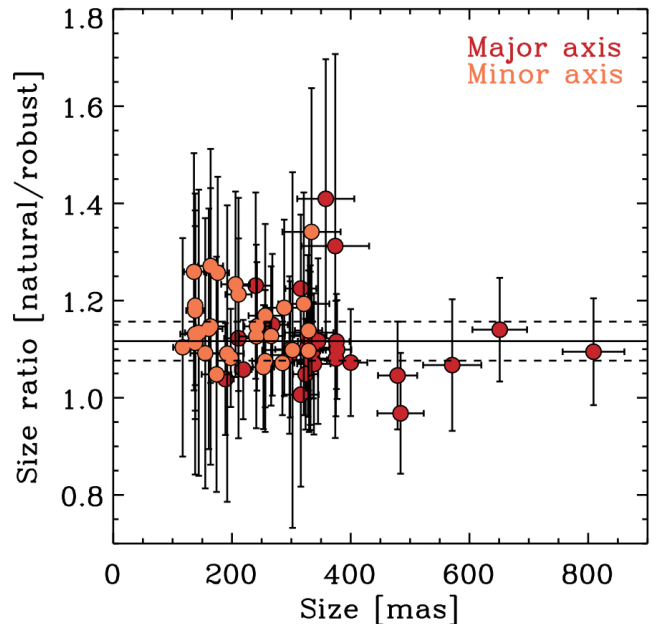


FIG. 6.— Ratio of the size of our ultrared DSFGs obtained with natural weighting and Briggs weighting with  $\text{ROBUST} = 0.5$  as a function of the ratio in the Briggs weighted maps with  $\text{ROBUST} = 0.5$ . The size ratio for the major and minor axis are plotted separately, as indicated in the color legend. We see that the sizes obtained using natural weighting are slightly higher than those obtained with Briggs weighting (as expected), by an average factor of  $1.12\times$ . We recall that the flux densities of our sources, on average, are  $1.17\times$  times higher when using natural weighting with respect to Briggs weighting and  $\text{ROBUST} = 0.5$  (see Fig. 1).

from the beam) of the components comprising each ultrared DSFG, in on-sky and physical units. We report the flux densities of all components detected at  $> 5\sigma$ , but report the size only of components detected at  $> 10\sigma$  because simulations have demonstrated that sizes of sources detected at  $< 10\sigma$  are not reliable (e.g. Simpson et al. 2015a; Hodge et al. 2016). In order to determine the size of each component in physical units (and also to determine luminosity distances and thence SFR – see later) we use spectroscopic redshifts when available. For sources without spectroscopic redshift, we have assumed the average photometric redshift of the sample,  $z_{\text{phot}} \sim 4.5$ . Assuming that our ultrared DSFGs lie  $z \sim 4.5$  introduces extra uncertainty on the size determination in physical units, because for the assumed cosmology the angular scale is  $7.3\ \text{kpc}''$  at  $z = 3.5$  and  $5.7\ \text{kpc}''$  at  $z = 6.0$ .

The SFR of each component (shown in Table 2) is calculated from its observed flux density assuming that the ALESS template provides a good representation of its FIR/submm SED (see §4 for a discussion on the uncertainties related to this assumption). It can be seen that the components of each ultrared DSFG are luminous starbursts, with  $\text{SFR} > 100\ M_{\odot}\ \text{yr}^{-1}$ , sometimes as high as  $\sim 2,400\ M_{\odot}\ \text{yr}^{-1}$ .

Fig. 7 shows the physical size of our ultrared DSFGs as a function of their observed, primary-beam-corrected flux densities at  $870\ \mu\text{m}$ . We show the size (FWHM) of the major axis, of the minor axis, and the average of the major and minor axes. We see evidence that brighter components are larger than smaller components. However, care should be taken when interpreting the size–

TABLE 2  
 PROPERTIES OF THE COMPONENTS SEEN IN THE UNLENSED, ULTRARED DSFGs

Source	$S_{B7}^{(a)}$ [mJy]	$A^a$ [mas $\times$ mas]	$A^a$ [kpc $\times$ kpc]	SFR [ $M_{\odot} \text{ yr}^{-1}$ ]	$\Sigma_{\text{SFR}}$ [ $M_{\odot} \text{ yr}^{-1} \text{ kpc}^{-2}$ ]
(RARE) HeLMS_54.1	14.7 $\pm$ 0.8	286 $\pm$ 17 $\times$ 210 $\pm$ 16	1.9 $\pm$ 0.1 $\times$ 1.4 $\pm$ 0.1	$\sim$ 1974	$\sim$ 945
(RARE) HeLMS_54.2	9.9 $\pm$ 0.2	191 $\pm$ 9 $\times$ 138 $\pm$ 11	1.3 $\pm$ 0.1 $\times$ 0.9 $\pm$ 0.1	$\sim$ 1329	$\sim$ 1447
(RARE) HeLMS_54.3	11.5 $\pm$ 0.7	409 $\pm$ 27 $\times$ 204 $\pm$ 19	2.7 $\pm$ 0.2 $\times$ 1.4 $\pm$ 0.1	$\sim$ 1544	$\sim$ 520
(RARE) HeLMS_54.4	1.4 $\pm$ 0.2	–	–	$\sim$ 188	–
(RARE) HeLMS_54.5	1.1 $\pm$ 0.3	–	–	$\sim$ 148	–
SGP-196076_1	17.58 $\pm$ 1.03	337 $\pm$ 25 $\times$ 298 $\pm$ 24	2.2 $\pm$ 0.2 $\times$ 2.0 $\pm$ 0.2	$\sim$ 2370	$\sim$ 686
SGP-196076_2	7.90 $\pm$ 0.60	309 $\pm$ 28 $\times$ 238 $\pm$ 24	2.0 $\pm$ 0.2 $\times$ 1.6 $\pm$ 0.2	$\sim$ 1060	$\sim$ 384
SGP-196076_3	1.33 $\pm$ 0.17	–	–	$\sim$ 180	–
SGP-354388_1	9.64 $\pm$ 0.33	255 $\pm$ 10 $\times$ 161 $\pm$ 10	1.8 $\pm$ 0.1 $\times$ 1.1 $\pm$ 0.1	$\sim$ 1301	$\sim$ 837
SGP-354388_2	3.61 $\pm$ 0.25	170 $\pm$ 17 $\times$ 54 $\pm$ 47	1.2 $\pm$ 0.2 $\times$ 0.4 $\pm$ 0.3	$\sim$ 487	$\sim$ 1015
SGP-354388_3	3.58 $\pm$ 0.16	74 $\pm$ 14 $\times$ 65 $\pm$ 15	0.5 $\pm$ 0.1 $\times$ 0.5 $\pm$ 0.1	$\sim$ 483	$\sim$ 1932
SGP-499646_1	1.91 $\pm$ 0.16	120 $\pm$ 17 $\times$ 58 $\pm$ 34	0.8 $\pm$ 0.1 $\times$ 1.5 $\pm$ 0.2	$\sim$ 161	$\sim$ 170
SGP-32338_1	9.05 $\pm$ 0.91	292 $\pm$ 40 $\times$ 268 $\pm$ 39	1.9 $\pm$ 0.3 $\times$ 1.8 $\pm$ 0.3	$\sim$ 1219	$\sim$ 454
SGP-32338_2	2.10 $\pm$ 0.25	–	–	$\sim$ 283	–
ELAISS1_40	4.74 $\pm$ 0.62	219 $\pm$ 37 $\times$ 168 $\pm$ 34	1.5 $\pm$ 0.2 $\times$ 1.1 $\pm$ 0.2	$\sim$ 639	$\sim$ 493
SGP-386447	7.33 $\pm$ 0.91	–	–	$\sim$ 739	–
SGP-93302	9.95 $\pm$ 0.90	260 $\pm$ 31 $\times$ 219 $\pm$ 28	1.7 $\pm$ 0.2 $\times$ 1.4 $\pm$ 0.2	$\sim$ 1340	$\sim$ 717
SGP-317726	4.74 $\pm$ 0.55	191 $\pm$ 31 $\times$ 167 $\pm$ 29	1.3 $\pm$ 0.2 $\times$ 1.1 $\pm$ 0.2	$\sim$ 640	$\sim$ 570
XMM_15	6.67 $\pm$ 0.36	207 $\pm$ 15 $\times$ 116 $\pm$ 13	1.4 $\pm$ 0.1 $\times$ 0.8 $\pm$ 0.1	$\sim$ 899	$\sim$ 1022
ADFS 17_1	7.73 $\pm$ 0.64	253 $\pm$ 27 $\times$ 109 $\pm$ 18	1.7 $\pm$ 0.2 $\times$ 0.7 $\pm$ 0.1	$\sim$ 1042	$\sim$ 1115
ADFS 17_2	5.29 $\pm$ 0.49	199 $\pm$ 27 $\times$ 104 $\pm$ 30	1.3 $\pm$ 0.2 $\times$ 0.7 $\pm$ 0.2	$\sim$ 713	$\sim$ 998
ADFS 17_3	4.97 $\pm$ 0.68	–	–	$\sim$ 670	–
ADFS 27_1	10.17 $\pm$ 0.83	271 $\pm$ 27 $\times$ 174 $\pm$ 23	1.8 $\pm$ 0.2 $\times$ 1.1 $\pm$ 0.1	$\sim$ 1367	$\sim$ 879
ADFS 27_2	9.83 $\pm$ 0.95	317 $\pm$ 34 $\times$ 127 $\pm$ 26	2.1 $\pm$ 0.2 $\times$ 0.8 $\pm$ 0.1	$\sim$ 1322	$\sim$ 1002
ADFS 31_1	10.53 $\pm$ 0.72	294 $\pm$ 23 $\times$ 185 $\pm$ 15	1.9 $\pm$ 0.2 $\times$ 1.2 $\pm$ 0.1	$\sim$ 1419	$\sim$ 793
ADFS 31_2	2.53 $\pm$ 0.30	–	–	$\sim$ 341	–
HeLMS_182	11.1 $\pm$ 0.7	247 $\pm$ 18 $\times$ 122 $\pm$ 12	1.6 $\pm$ 0.1 $\times$ 0.8 $\pm$ 0.1	$\sim$ 1492	$\sim$ 1485
ELAISS1_18_1	11.2 $\pm$ 0.9	471 $\pm$ 41 $\times$ 233 $\pm$ 24	3.1 $\pm$ 0.3 $\times$ 1.5 $\pm$ 0.2	$\sim$ 1506	$\sim$ 413
ELAISS1_18_2	4.0 $\pm$ 0.4	205 $\pm$ 28 $\times$ 184 $\pm$ 30	1.4 $\pm$ 0.2 $\times$ 1.2 $\pm$ 0.2	$\sim$ 538	$\sim$ 408
ELAISS1_26	8.63 $\pm$ 0.58	233 $\pm$ 20 $\times$ 167 $\pm$ 17	1.5 $\pm$ 0.1 $\times$ 1.1 $\pm$ 0.1	$\sim$ 1160	$\sim$ 896
SGP-72464	13.23 $\pm$ 0.92	347 $\pm$ 28 $\times$ 236 $\pm$ 22	2.3 $\pm$ 0.2 $\times$ 1.6 $\pm$ 0.1	$\sim$ 1779	$\sim$ 616
SGP-392029.1	5.15 $\pm$ 0.28	182 $\pm$ 15 $\times$ 124 $\pm$ 13	1.2 $\pm$ 0.1 $\times$ 0.8 $\pm$ 0.1	$\sim$ 692	$\sim$ 918
SGP-392029.2	3.11 $\pm$ 0.24	188 $\pm$ 27 $\times$ 166 $\pm$ 30	1.2 $\pm$ 0.2 $\times$ 1.1 $\pm$ 0.2	$\sim$ 418	$\sim$ 403
SGP-135338	5.06 $\pm$ 0.28	307 $\pm$ 20 $\times$ 106 $\pm$ 16	2.0 $\pm$ 0.1 $\times$ 0.7 $\pm$ 0.1	$\sim$ 680	$\sim$ 619
SGP-213813	9.84 $\pm$ 0.87	535 $\pm$ 50 $\times$ 219 $\pm$ 26	3.5 $\pm$ 0.3 $\times$ 1.4 $\pm$ 0.2	$\sim$ 1323	$\sim$ 344
G09-80620.1	5.08 $\pm$ 0.97	–	–	$\sim$ 683	–
G09-80620.2	1.45 $\pm$ 0.29	–	–	$\sim$ 195	–
G09-80658.1	4.08 $\pm$ 0.40	309 $\pm$ 36 $\times$ 143 $\pm$ 28	2.0 $\pm$ 0.2 $\times$ 0.9 $\pm$ 0.2	$\sim$ 549	$\sim$ 389
G09-80658.2	1.35 $\pm$ 0.13	139 $\pm$ 35 $\times$ 53 $\pm$ 26	0.9 $\pm$ 0.2 $\times$ 0.3 $\pm$ 0.2	$\sim$ 181	$\sim$ 854
G09-79552	10.09 $\pm$ 0.85	273 $\pm$ 29 $\times$ 214 $\pm$ 25	1.8 $\pm$ 0.2 $\times$ 1.4 $\pm$ 0.2	$\sim$ 1357	$\sim$ 686
G09-59393.1	7.33 $\pm$ 0.48	373 $\pm$ 28 $\times$ 117 $\pm$ 16	2.5 $\pm$ 0.2 $\times$ 0.8 $\pm$ 0.1	$\sim$ 985	$\sim$ 627
G09-59393.2	3.25 $\pm$ 0.64	–	–	$\sim$ 437	–
HELMS_RED_68.1	6.06 $\pm$ 0.54	500 $\pm$ 50 $\times$ 141 $\pm$ 23	3.3 $\pm$ 0.3 $\times$ 0.9 $\pm$ 0.1	$\sim$ 814	$\sim$ 349
HELMS_RED_68.2	16.5 $\pm$ 2.2	314 $\pm$ 51 $\times$ 176 $\pm$ 42	2.1 $\pm$ 0.3 $\times$ 1.2 $\pm$ 0.2	$\sim$ 2218	$\sim$ 1121
HELMS_RED_270.1	7.94 $\pm$ 0.61	458 $\pm$ 37 $\times$ 238 $\pm$ 24	3.0 $\pm$ 0.2 $\times$ 1.6 $\pm$ 0.2	$\sim$ 1067	$\sim$ 283
HELMS_RED_270.2	5.73 $\pm$ 0.51	291 $\pm$ 32 $\times$ 242 $\pm$ 28	1.9 $\pm$ 0.2 $\times$ 1.6 $\pm$ 0.2	$\sim$ 770	$\sim$ 323
SGP-385891.1	5.9 $\pm$ 0.3	358 $\pm$ 22 $\times$ 134 $\pm$ 15	2.4 $\pm$ 0.1 $\times$ 0.9 $\pm$ 0.1	$\sim$ 579	$\sim$ 341
SGP-385891.2	1.5 $\pm$ 0.2	–	–	$\sim$ 147	–

<sup>a</sup>Measured in the primary-beam-corrected maps

<sup>a</sup>The reported values are  $\text{FWHM}_{\text{major}} \times \text{FWHM}_{\text{minor}}$ , where  $\text{FWHM}_{\text{major}}$  and  $\text{FWHM}_{\text{minor}}$  are obtained from a two-dimensional elliptical Gaussian profile fit to the observed emission. We only report the size of sources detected at  $> 10\sigma$  at  $870 \mu\text{m}$  before primary-beam correction. In order to derive the physical size in kpc for sources without spectroscopic redshift we have assumed  $z = 4.5$ .

flux relation: the faintest galaxies might have smaller sizes because the observations are not deep enough to detect any faint extended emission. However, any bright ( $S_{870} > 15 \text{ mJy}$ ) and relatively compact ( $\lesssim 1.5 \text{ kpc}$ ) galaxies should have been found. They are not present in our sample. We see a wide range of sizes for a fixed flux density, especially in the flux density range  $5 < S_{870} [\text{mJy}] < 10$ , with an average size for our ultra-red DSFGs,  $\theta_{\text{FWHM}} = 1.46 \pm 0.41 \text{ kpc}$ .

We also show in Fig. 7 the sizes of luminous DSFGs at

$z \sim 2.5$  selected from the ALESS survey (Karim et al. 2013; Hodge et al. 2013) derived by Hodge et al. (2016) with dust continuum observations at a spatial resolution (in sky units) comparable to ours. Note that we exclude from the Hodge et al. (2016) sample one source without a spectroscopic redshift and another source with  $z_{\text{spec}} < 1$ . Notably, the average size of the DSFGs in Hodge et al. (2016) is  $2\times$  larger than the average value found in this work. We have divided the Hodge et al. (2016) sample into two redshift ranges: sources whose redshifts are



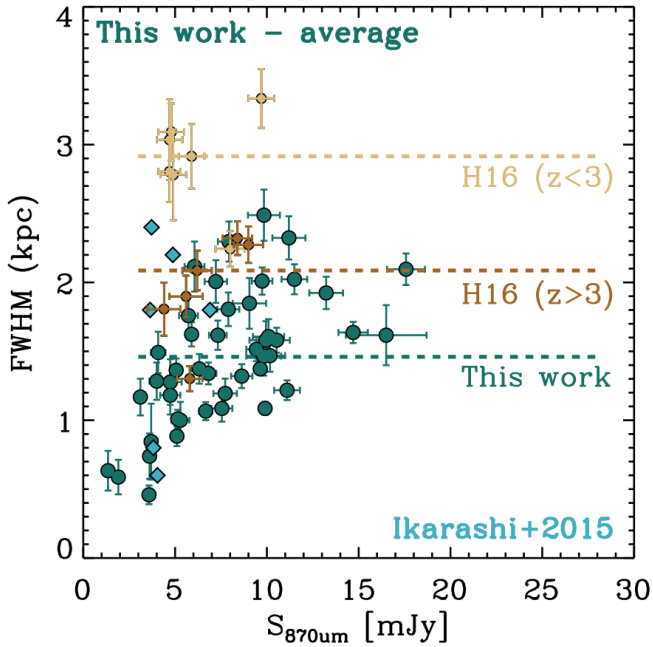


FIG. 7.— Size of our ultrared DSFGs as a function of their primary-beam-corrected flux densities at  $870\ \mu\text{m}$ . We include in this figure the average of the major and minor axes, each calculated from a 2D Gaussian fit to the dust continuum emission. The values reported correspond to the FWHM of the Gaussian fits. For comparison we also represent the size of the SMGs studied in Ikarashi et al. (2015) and Hodge et al. (2016). We distinguish between sources at  $z_{\text{spec}} < 3.0$  and  $z_{\text{spec}} > 3.0$  in the Hodge et al. (2016) sample. The flux densities in Ikarashi et al. (2015) were derived at  $\sim 1.1\ \text{mm}$  and have been converted to flux densities at  $\sim 870\ \mu\text{m}$  by multiplying them by  $\times 1.5$ . The average values found in Hodge et al. (2016) and this work are indicated with the horizontal dashed lines. We see that DSFGs at higher redshifts tend to have smaller sizes, on average.

greater than and less than  $z_{\text{spec}} = 3.0$  and it can be seen that the dust emission for DSFGs at lower redshift is more extended than for those at higher redshifts. Ikarashi et al. (2015) reported the dust continuum sizes for a sample of AzTEC-selected SMGs at  $z_{\text{phot}} > 2.8$ , although they are likely at lower redshift than our ultrared DSFGs given their bluer SPIRE colors. Despite the differences, the sizes reported in Ikarashi et al. (2015) are similar to those for our ultrared DSFGs. In this comparison we have only used the six sources in Ikarashi et al. (2015) with observations at a resolution similar to that in our work, since the resolution for the other galaxies is too low ( $\sim 0.7''$ ) to allow a fair comparison. Our derived sizes are also smaller than the size of DSFGs at  $z \sim 1-3$  measured via high-resolution radio continuum imaging (Biggs & Ivison 2008) or in high- $J$  CO emission lines (Tacconi et al. 2006).

The combination of all previous results show that DSFGs tend to be smaller in the early Universe,  $z = 4-6$ , than at ‘cosmic noon’ – the peak of cosmic star formation,  $z \sim 2-3$ .

### 6.3. SFR surface density

In this section we discuss the SFR surface density ( $\Sigma_{\text{SFR}}$ ) of our galaxies, which have been calculated as:  $\Sigma_{\text{SFR}} = \text{SFR}/A_{\text{dust}}$ , where the area of the dust emission,  $A_{\text{dust}}$ , has been obtained from  $\pi \times R_a \times R_b$ , where

$R_a$  and  $R_b$  are the semi-major and semi-minor axis, respectively, calculated as  $R_a = 0.5 \times \text{FWHM}_{\text{major}}$  and  $R_b = 0.5 \times \text{FWHM}_{\text{minor}}$ . This is the same definition used in Oteo et al. (2016a), Riechers et al. (2014) and several other works analyzing the properties of dust emission in luminous starbursts at high redshift. However, we note that some other work, e.g. Simpson et al. (2015a); Oteo et al. (2017c), used the definition  $\Sigma'_{\text{SFR}} = 0.5 \times \text{SFR}/A_{\text{dust}}$  to take into account that FWHM measures the size where half of the total SFR is taking place. The difference between the two definitions is relevant when comparing different samples in the literature.

We find a noticeable range of  $\Sigma_{\text{SFR}}$  in our ultrared DSFGs, from  $\sim 150$  to  $\sim 2,000\ M_{\odot}\ \text{yr}^{-1}\ \text{kpc}^{-2}$  (see values in Table 2). Remarkably, 14 of our unlensed ultrared DSFGs have  $\Sigma_{\text{SFR}} > 800\ M_{\odot}\ \text{yr}^{-1}\ \text{kpc}^{-2}$  and are therefore at – or are close to – the Eddington limit (Thompson et al. 2005). We have already discussed the Eddington-limited nature of SGP-196076.1 in Oteo et al. (2016a). Despite its high  $\Sigma_{\text{SFR}}$ , there is no sign of outflows in the CO or [C II] emission, and the OH  $163\ \mu\text{m}$  transition (a tracer of molecular outflows – Spoon et al. 2013) is weak. SGP-354388 and ADFS 17 are interesting cases, since two of their interacting components are Eddington-limited starbursts.

It should be noted that determining  $\Sigma_{\text{SFR}}$  accurately for DSFGs requires us to measure the extent of their dust emission accurately and, thus, on the availability of observations with sufficient resolution to resolve individual star-forming clumps. Some of the apparently smooth disks could be resolved into different star-forming clumps if observed at higher resolution. This was, for example, the case for ALMACAL-1 and ALMACAL-2 (Oteo et al. 2017c), the two brightest SMGs found in the ALMACAL survey (Oteo et al. 2016b). Using high spatial resolution ( $\sim 0.4''$ ) data we derived an SFR surface density of  $\sim 165\ M_{\odot}\ \text{yr}^{-1}\ \text{kpc}^{-2}$  in ALMACAL-1. However, ultra-high spatial resolution (beam size  $\sim 20\ \text{mas}$ ) observations revealed that the sources are actually extremely compact and have enormous SFRs, meaning the SFR surface density is as high as  $\sim 6,000\ M_{\odot}\ \text{yr}^{-1}\ \text{kpc}^{-2}$ .

### 6.4. From ultrared DSFGs to local ultra-massive ellipticals

Having confirmed the existence of a population of DSFGs with extreme IR luminosities and SFRs at  $z \sim 4-6$ , we now explore the possible future evolution of these systems.

Given the relatively wide range of morphologies and spatial extents of our ultrared DSFGs (see §6.1), the interpretation is challenging for many sources. There are ultrared DSFGs which are resolved into different sub-components separated by several arcsec (ADFS 17, ADFS 31, or SGP-93302 – see Figs. 8 to 9). Without spectroscopic confirmation it is not possible to know whether all these galaxies are at the same redshift and are, therefore, physically associated. On the other hand, there are sources that – due to their close proximity – are likely the components of a merger of several dusty galaxies. Examples include SGP-196076 (where the interaction has been confirmed via detection of CO and [C II] in two of the galaxies – Oteo et al. 2016a), SGP-354388, ADFS 27 and ELASS1 18. The physical re-

lation between close components is further supported by the submm number counts (see for example Simpson et al. 2015b; Oteo et al. 2016b), since the probability of finding such bright sources so close to each other is very low.

In order to study the likely evolution of our ultrared DSFGs we would ideally need  $^{12}\text{CO}(1-0)$  or  $[\text{C I}](1-0)$  detections to measure their molecular gas mass which, in combination with their total SFRs, provide estimates of their gas-depletion times (always assuming a standard IMF, cf. Romano et al. 2017, who claim  $L_{\text{IR}}$ -derived SFRs in starbursts might be up to  $5\times$  too high). In Oteo et al. (2016a) we estimated the gas-depletion time for one of our sources with mid- $J$  CO detections and concluded that – in the absence of an external molecular gas supply – this source would likely become a massive elliptical by  $z \sim 3$ . The same would happen to ADSF.27 according to the gas-depletion time derived by Riechers et al. (2017). Our galaxies lack of CO data, for the most part, but we can estimate the gas-depletion time using the relatively tight relation between the dust continuum luminosity at rest-frame  $850\ \mu\text{m}$  and the  $^{12}\text{CO}(1-0)$  luminosity (e.g. Scoville et al. 2016; Hughes et al. 2017; Oteo et al. 2017b) with the caution that this relation has not been tested for galaxies in our redshift and luminosity ranges. We have estimated the rest-frame  $850\ \mu\text{m}$  luminosity of our sources by assuming the ALESS template, providing some consistency with the procedure we followed to estimate their SFR. The average flux density of our sources at  $870\ \mu\text{m}$  is  $7.7\ \text{mJy}$ . Assuming that the average redshift of our sources is  $z = 4.5$ , the average total SFR would then be  $\text{SFR} \sim 760\ M_{\odot}\ \text{yr}^{-1}$  and the molecular gas mass  $M_{\text{gas}} \sim 3.2 \times 10^{11}\ M_{\odot}$ . This implies a gas-depletion time of  $420\ \text{Myr}$  and that all the molecular gas available for star formation will be consumed by  $z \sim 3$ . Therefore, if there is no external gas supply, our ultrared DSFGs will evolve into massive elliptical-like galaxies at  $z \sim 3-3.5$ , with stellar masses of at least  $M_{\text{stars}} = 3.2 \times 10^{11}\ M_{\odot}$ .

Extensive work on the analysis of the stellar populations in local elliptical galaxies has shown that the more massive a galaxy is, the earlier it should have been formed. In particular, most massive galaxies with  $M_{\text{star}} > 5 \times 10^{11}\ M_{\odot}$  in the local Universe formed most of their stars at  $z > 2$  in a relatively fast and intense burst of star formation, which could range in duration between  $\sim 1\ \text{Gyr}$  to a few million years for the most massive galaxies (Thomas et al. 2010). Along the same lines, the existence of a population of massive, red-and-dead galaxies at  $z \sim 2$  implies an early formation epoch (Krogager et al. 2014), a phase which is consistent with the extreme SFRs found in our ultrared DSFGs (Toft et al. 2014). Taking together, our results suggest that ultrared DSFGs evolve into the most massive galaxies at  $z \sim 3$ , which are the progenitors of the already quiescent population at  $z \sim 2$  which, in turn, are the progenitors of local ultra-massive galaxies. This scenario is similar to the one proposed by Ikarashi et al. (2015) for their sample of SMGs, which are less luminous and are likely at lower redshift than our ultrared DSFGs. Therefore, the combination of previous results (both from observations and simulations) and our results suggests that a population of elliptical galaxies has been formed in intense high-redshift starbursts, represented by different SMG

phases. The most massive galaxies in the local Universe formed in an SMG phase at  $z \sim 4-6$ , compatible with our ultrared DSFGs, whereas less massive local elliptical galaxies also formed in an SMG phase but less intense and at lower redshifts.

The measured sizes of our ultrared DSFGs are also in agreement with a scenario where these sources will evolve into the most massive ellipticals at  $z \sim 3$ . Most ultrared DSFGs have physical sizes below  $2.5\ \text{kpc}$  (there is only one source with an average size larger than  $3\ \text{kpc}$ ). The evolution from ultrared DSFGs to massive ellipticals is further supported by the analysis of the stellar populations of massive quiescent galaxies at  $z \sim 2$  carried out in Krogager et al. (2014), which showed that the formation epoch of some of those sources is compatible with  $z > 4$ , comparable to the redshift distribution of our ultrared DSFGs. The sizes of the massive ellipticals in Krogager et al. (2014) are as large as  $4.5\ \text{kpc}$ , larger than all our ultrared DSFGs and, therefore, even the largest galaxy in our sample is compatible with a size evolution in which quiescent galaxies at  $z \sim 3$  are the descendants of smaller DSFGs at higher redshifts that increase their size while or after their star formation ceases. This evolutionary picture is also compatible with the one proposed by Barro et al. (2016) for the formation of compact quiescent galaxies at  $z \sim 2$ , which would be a scaled-down population in terms of redshift and mass of both the progenitors and descendants and luminosities of the progenitors.

## 7. CONCLUSIONS

In this paper we have presented high-spatial-resolution ( $\sim 0.12''$  or  $\approx 800\ \text{pc}$ ) ALMA  $870\ \mu\text{m}$  dust continuum observations of a sample of 44 ultrared DSFGs. These were taken from the *H-ATLAS* and *HerMES* surveys, selected to have red SPIRE colors, consistent with them being at  $z \sim 4-6$ . Our main conclusions are:

1. We have confirmed that there exists a significant population of unlensed ultrared DSFGs which are among the most luminous sources found so far in the early Universe, forming stars at tremendous rates, up to a collective  $\text{SFR} \sim 4,500\ M_{\odot}\ \text{yr}^{-1}$  when we coadd the different sub-components into which ultrared DSFGs are resolved, and up to  $\text{SFR} \sim 2,400\ M_{\odot}\ \text{yr}^{-1}$  for individual components.
2. The lower limits on the number counts of ultrared DSFGs at  $500\ \mu\text{m}$  (where flux densities have been measured from SPIRE) conflict with models expectations, but not at  $870\ \mu\text{m}$  (where flux densities have been measured from ALMA, after refinement of the samples with SCUBA-2 and LABOCA). This can be explained by the lack of correction for flux boosting in the SPIRE flux densities, by the effect of clustering in the large SPIRE beams, or by a combination of both. These problems do not affect ALMA, although the relatively small ALMA field of view means we might miss some emission, especially in sources with extended LABOCA emission.
3. We find a variety of dust continuum morphologies, from relatively smooth disks with extended star formation to compact sources, both isolated, and interacting. The average FWHM size of the

dust continuum in our ultrared DSFGs is  $\sim 1.46 \pm 0.41$  kpc, so smaller than the values reported in DSFGs at lower redshifts.

4. The fact that the average size of our ultrared DSFGs is lower than that found for massive quiescent galaxies at  $z \sim 2-3$  supports the idea that the former are the progenitors of the latter. This is further supported by the expected short gas-depletion time of our ultrared DSFGs, as their star formation would cease after a few hundred million years. We are thus witnessing the birth of the high-mass end of the red sequence of galaxies.

IO, RJI, LD and AJRL acknowledge support from the European Research Council (ERC) in the form of the Advanced Investigator Programme, 321302, COSMICISM. MN acknowledges financial support from the European Union's Horizon 2020 research and innovation programme under the Marie Skłodowska-Curie grant agreement No. 707601. IRS acknowledges support from STFC (ST/P000541/1), the ERC Advanced Investigator programme, 321334, DUSTYGAL and a Royal Society

Wolfson Merit Award. HD acknowledges financial support from the Spanish Ministry of Economy and Competitiveness (MINECO) under the 2014 Ramón y Cajal programme MINECO RYC-2014-15686. MJM acknowledges the support of the National Science Centre, Poland, through the POLONEZ grant 2015/19/P/ST9/04010. This project has received funding from the European Union's Horizon 2020 research and innovation programme under the Marie Skłodowska-Curie grant agreement No. 665778. DR acknowledges support from the National Science Foundation under grant number AST-1614213. This paper makes use of the following ALMA data: ADS/JAO.ALMA#2013.1.00001.S and ADS/JAO.ALMA#2016.1.00139.S. ALMA is a partnership of ESO (representing its member states), NSF (USA) and NINS (Japan), together with NRC (Canada) and NSC and ASIAA (Taiwan) and KASI (Republic of Korea), in cooperation with the Republic of Chile. The Joint ALMA Observatory is operated by ESO, AUI/NRAO and NAOJ. *H-ATLAS* is a project with *Herschel*, which is an ESA space observatory with science instruments provided by European-led Principal Investigator consortia and with important participation from NASA. The *H-ATLAS* website is <http://www.h-atlas.org/>.

## REFERENCES

- Asboth V. et al., 2016, MNRAS, 462, 1989  
 Baldry I. K., Glazebrook K., Brinkmann J., Ivezić Ž., Lupton R. H., Nichol R. C., Szalay A. S., 2004, ApJ, 600, 681  
 Barro G. et al., 2016, ApJ, 827, L32  
 Biggs A. D., Ivison R. J., 2008, MNRAS, 385, 893  
 Blanton M. R. et al., 2003, ApJ, 594, 186  
 Bourne N. et al., 2016, MNRAS, 462, 1714  
 Bower R. G., Lucey J. R., Ellis R. S., 1992a, MNRAS, 254, 601  
 Bower R. G., Lucey J. R., Ellis R. S., 1992b, MNRAS, 254, 589  
 Brammer G. B. et al., 2009, ApJ, 706, L173  
 Cai Z.-Y. et al., 2013, ApJ, 768, 21  
 Capak P. et al., 2008, ApJ, 681, L53  
 Casey C. M., Narayanan D., Cooray A., 2014, Phys. Rep., 541, 45  
 Collins C. A. et al., 2009, Nature, 458, 603  
 Combes F. et al., 2012, A&A, 538, L4  
 Coppin K. et al., 2006, MNRAS, 372, 1621  
 Coppin K. E. K. et al., 2009, MNRAS, 395, 1905  
 Cox P. et al., 2011, ApJ, 740, 63  
 Daddi E. et al., 2009, ApJ, 694, 1517  
 Dowell C. D. et al., 2014, ApJ, 780, 75  
 Dunne L., Eales S., Edmunds M., Ivison R., Alexander P., Clements D. L., 2000, MNRAS, 315, 115  
 Eales S. et al., 2010, PASP, 122, 499  
 Edge A., Sutherland W., Kuijken K., Driver S., McMahon R., Eales S., Emerson J. P., 2013, The Messenger, 154, 32  
 Farrah D., Afonso J., Efstathiou A., Rowan-Robinson M., Fox M., Clements D., 2003, MNRAS, 343, 585  
 Fudamoto Y. et al., 2017, ArXiv e-prints  
 Geach J. E. et al., 2017, MNRAS, 465, 1789  
 Gobat R. et al., 2011, A&A, 526, A133  
 Griffin M. J. et al., 2010, A&A, 518, L3+  
 Hodge J. A., Carilli C. L., Walter F., de Blok W. J. G., Riechers D., Daddi E., Lentati L., 2012, ApJ, 760, 11  
 Hodge J. A. et al., 2013, ApJ, 768, 91  
 Hodge J. A. et al., 2016, ApJ, 833, 103  
 Hughes T. M. et al., 2017, MNRAS, 468, L103  
 Hwang H. S. et al., 2010, MNRAS, 409, 75  
 Ikarashi S. et al., 2015, ApJ, 810, 133  
 Ivison R. J. et al., 2016, ApJ, 832, 78  
 Ivison R. J. et al., 2013, ApJ, 772, 137  
 Ivison R. J. et al., 2010, A&A, 518, L35  
 Karim A. et al., 2013, MNRAS, 432, 2  
 Kennicutt, Jr. R. C., 1998, ARA&A, 36, 189  
 Knudsen K. K., Kneib J.-P., Richard J., Petitpas G., Egami E., 2010, ApJ, 709, 210  
 Knudsen K. K., van der Werf P. P., Kneib J.-P., 2008, MNRAS, 384, 1611  
 Krogager J.-K., Zirm A. W., Toft S., Man A., Brammer G., 2014, ApJ, 797, 17  
 Labbé I. et al., 2005, ApJ, 624, L81  
 Lapi A. et al., 2011, ApJ, 742, 24  
 Nayyeri H. et al., 2017, ArXiv e-prints  
 Nayyeri H. et al., 2014, ApJ, 794, 68  
 Negrello M. et al., 2017, MNRAS, 465, 3558  
 Negrello M. et al., 2010, Science, 330, 800  
 Oliver S. J. et al., 2010, A&A, 518, L21  
 Oteo I. et al., 2017a, ArXiv e-prints  
 Oteo I. et al., 2016a, ApJ, 827, 34  
 Oteo I. et al., 2017b, ArXiv e-prints  
 Oteo I., Zwaan M. A., Ivison R. J., Smail I., Biggs A. D., 2016b, ApJ, 822, 36  
 Oteo I., Zwaan M. A., Ivison R. J., Smail I., Biggs A. D., 2017c, ApJ, 837, 182  
 Pearson E. A. et al., 2013, MNRAS, 435, 2753  
 Petty S. M. et al., 2013, AJ, 146, 77  
 Pilbratt G. L. et al., 2010, A&A, 518, L1  
 Pope A. et al., 2008, ApJ, 675, 1171  
 Riechers D. A. et al., 2013, Nature, 496, 329  
 Riechers D. A. et al., 2014, ApJ, 796, 84  
 Riechers D. A. et al., 2017, ArXiv e-prints  
 Romano D., Matteucci F., Zhang Z.-Y., Papadopoulos P. P., Ivison R. J., 2017, MNRAS, 470, 401  
 Rood H. J., 1969, ApJ, 158, 657  
 Scoville N. et al., 2016, ApJ, 820, 83  
 Simpson J. M. et al., 2015a, ApJ, 799, 81  
 Simpson J. M. et al., 2015b, ApJ, 807, 128  
 Smail I., Swinbank A. M., Ivison R. J., Ibar E., 2011, MNRAS, 414, L95  
 Smolčić V. et al., 2011, ApJ, 731, L27  
 Smolčić V. et al., 2015, A&A, 576, A127  
 Spoon H. W. W. et al., 2013, ApJ, 775, 127  
 Strateva I. et al., 2001, AJ, 122, 1861  
 Swinbank A. M. et al., 2012, MNRAS, 427, 1066  
 Swinbank A. M. et al., 2014, MNRAS, 438, 1267  
 Swinbank A. M. et al., 2010, Nature, 464, 733  
 Tacconi L. J. et al., 2006, ApJ, 640, 228

- Thomas D., Maraston C., Schawinski K., Sarzi M., Silk J., 2010, MNRAS, 404, 1775
- Thompson T. A., Quataert E., Murray N., 2005, ApJ, 630, 167
- Toft S. et al., 2014, ApJ, 782, 68
- Valiante E. et al., 2016, MNRAS, 462, 3146
- Whitaker K. E. et al., 2011, ApJ, 735, 86
- Williams R. J., Quadri R. F., Franx M., van Dokkum P., Labbé I., 2009, ApJ, 691, 1879
- Yun M. S. et al., 2015, MNRAS, 454, 3485
- Zavala J. A. et al., 2017, ArXiv e-prints
- Zeimann G. R. et al., 2012, ApJ, 756, 115

## APPENDIX



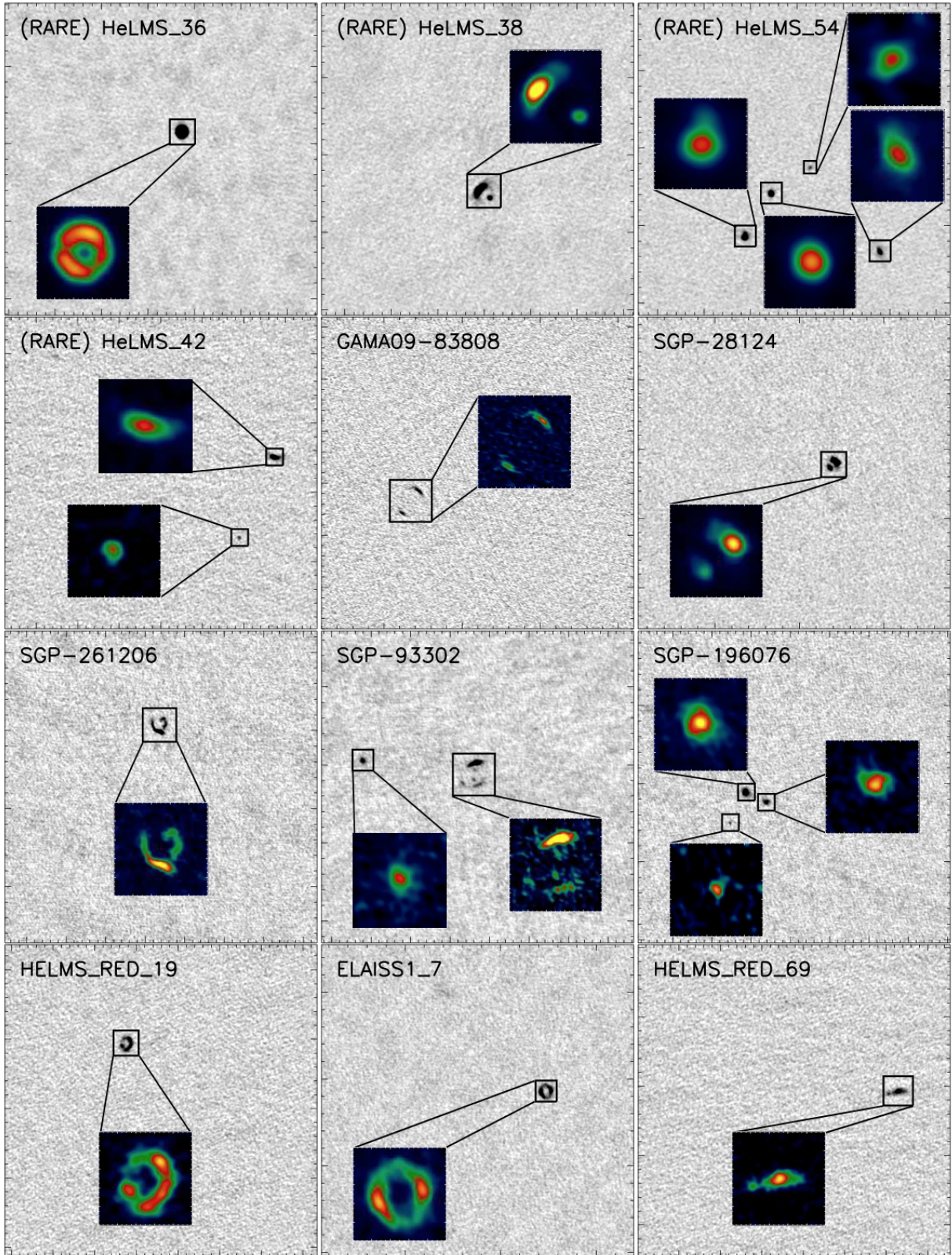


FIG. 8.— ALMA 870  $\mu\text{m}$  imaging of our UR galaxies at  $\sim 0.1''$  (or 800 pc) spatial resolution. We show on each image the area covered by the primary beam to show all components which our UR starbursts are split into. On each image we include an inset figure to highlight the dust emission morphology of each detected component.



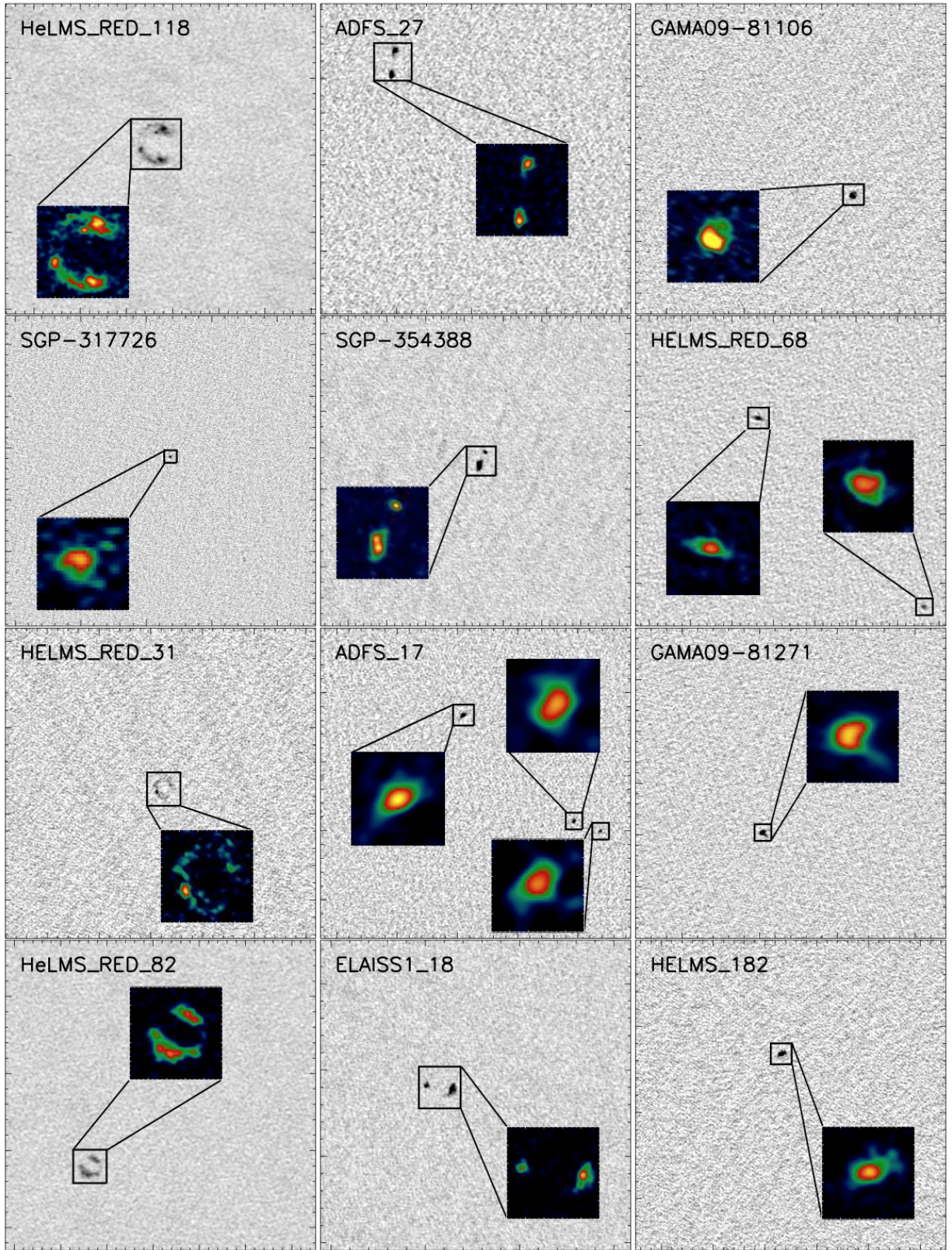


FIG. 9.— ALMA 870  $\mu\text{m}$  imaging of our UR galaxies at  $\sim 0.1''$  (or 800 pc) spatial resolution. We show on each image the area covered by the primary beam to show all components which our UR starbursts are split into. On each image we include an inset figure to highlight the dust emission morphology of each detected component.



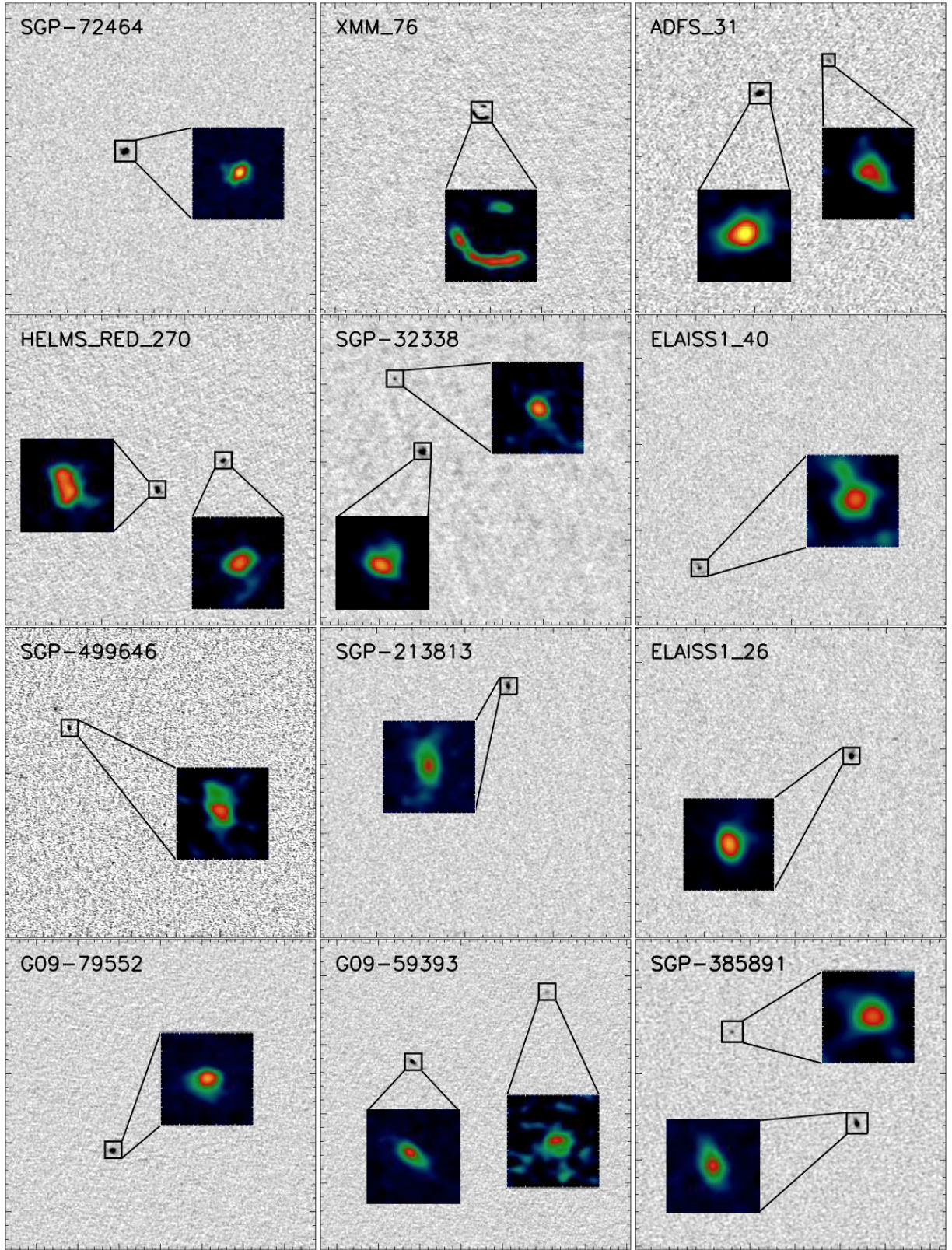


FIG. 10.— ALMA 870  $\mu\text{m}$  imaging of our UR galaxies at  $\sim 0.1''$  (or 800 pc) spatial resolution. We show on each image the area covered by the primary beam to show all components which our UR starbursts are split into. On each image we include an inset figure to highlight the dust emission morphology of each detected component.



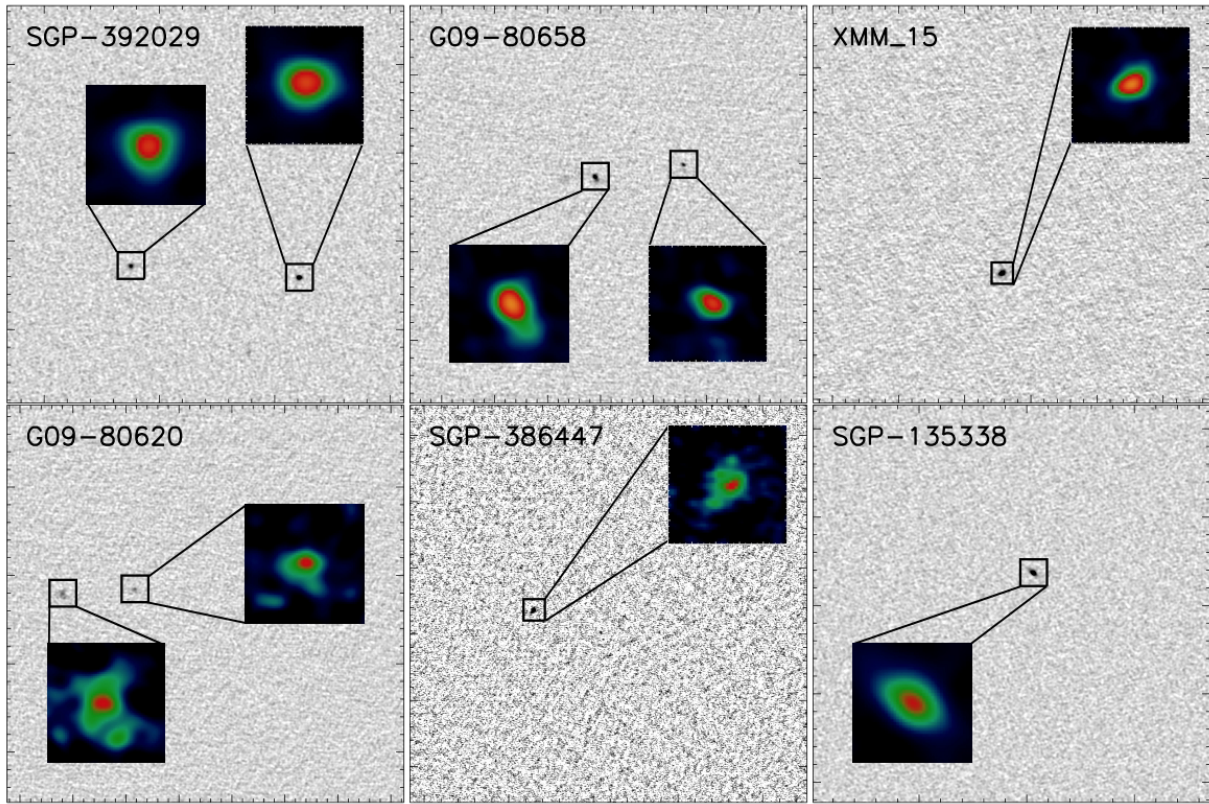


FIG. 11.— ALMA 870  $\mu\text{m}$  imaging of our UR galaxies at  $\sim 0.1''$  (or 800 pc) spatial resolution. We show on each image the area covered by the primary beam to show all components which our UR starbursts are split into. On each image we include an inset figure to highlight the dust emission morphology of each detected component.